



**KWANTEACH®**



PARTIAL

# Table of Contents

1. About this manual .....	6
2. Introduction .....	8
2.1. NV centres in diamonds .....	8
2.2. NV centre orientation .....	8
2.3. Spin properties .....	9
2.4. Optical bench .....	13
2.5. Spin manipulation .....	13
3. Base module: setting up and alignment .....	21
3.1. General installation .....	21
3.2. Mounting parts .....	21
4. Optically Detected Magnetic Resonance (ODMR) .....	28
4.1. Theoretical principles .....	28
4.2. Experimental protocol .....	28
5. Observation of the Zeeman effect at low field .....	30
5.1. Theoretical principles .....	30
6. Observation of hyperfine lines .....	39
6.1. Theoretical principles .....	39
6.2. Experimental protocol .....	40
7. Earth field measurement .....	44
7.1. Theoretical principles .....	44
7.2. Experimental protocol .....	46
8. Noise analysis and system sensitivity calculation .....	51
8.1. Theoretical principles .....	51
8.2. Experimental protocol .....	53
8.3. Numerical applications .....	55
9. Observation of strong-field level mixing .....	57
9.1. Theoretical principles .....	57
9.2. Experimental protocol .....	57
10. Pulsed module: setting up and alignment .....	59
10.1. General installation .....	59
11. Saturation of NV centers .....	64
11.1. Theoretical principles .....	64
11.2. Experimental protocol .....	64
12. Polarisation and relaxation time $T_1$ of the NV centre .....	66
12.1. Theoretical principles .....	66
12.2. Experimental protocol .....	68

13. Microwave Pulse Delay Calibration .....	76
13.1. Context .....	76
14. Rabi Oscillations .....	78
14.1. Theoretical principles .....	78
14.2. Rabi oscillations with NV centres ensemble .....	78
15. Ramsey fringes .....	84
15.1. Theoretical principles .....	84
15.2. Experimental protocol .....	88
16. Spin Echo .....	93
17. Contact information .....	94

PARTIAL

**AVERTISSEMENT**

Ce Manuel Technique est mis à disposition de l'Enseignant et de l'équipe pédagogique en charge d'animer le module de travaux pratiques sur les technologies quantiques utilisant l'équipement KWANTEACH®. L'usage de ce Manuel est individuel et strictement réservé aux manipulations mettant en œuvre le KWANTEACH®. La diffusion de tout ou partie de ce document doit faire l'objet d'un accord express de KWAN-TEK ©.

**WARNING**

This Technical Manual is made available to the Teacher and the teaching crew in charge of leading the practical work module on quantum technologies using the KWANTEACH® equipment. The use of this Manual is individual and strictly reserved for manipulations using the KWANTEACH®. Distribution of all or part of this document is subject to the express agreement of KWAN-TEK ©.

PARTIAL

## 1. About this manual

There is an increasing need for qualified technicians, engineers and scientists in the field of quantum mechanics technologies, driven by the new growing markets of quantum information, computing and sensing.

To meet future research and workforce demands in quantum physics, we need to overcome the challenge of educating and training students, by expanding the offer in practical works especially on the engineering side.

Through its expertise in quantum sensor development, KWAN-TEK has developed an education kit: KWANTEACH®. Based on NV centres in diamonds, KWANTEACH® is an easy-to-use system. It allows students to concretely approach theoretical concepts of atomic and quantum physics, such as the interaction of matter with electromagnetic fields, the fine and hyperfine structure of atoms, the Zeeman effect,..., as well as to perform optical alignment, to characterize the sensitivity of a quantum sensor, to understand qubit manipulations, between others. These are key techniques in the practical implementations of many quantum systems, to elaborate quantum technologies.

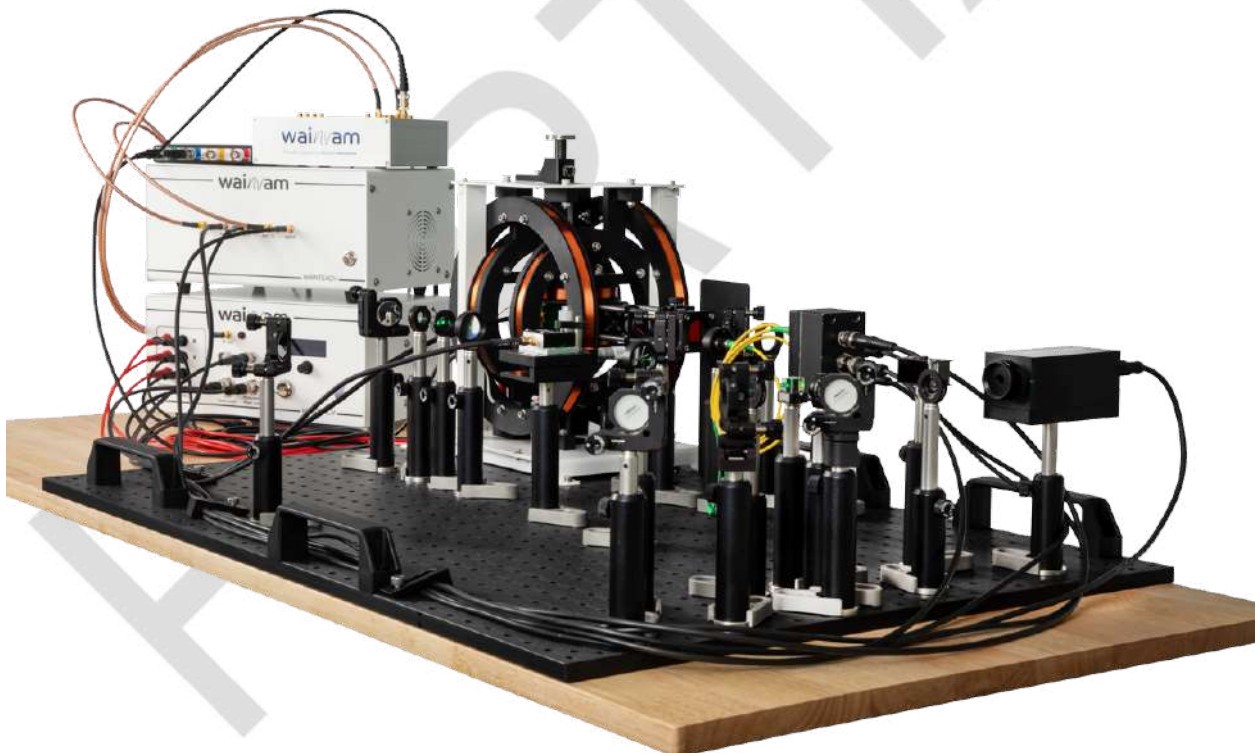


*Figure 1. KWANTEACH® education kit*



## Version Control

*Table 1. List of changes*

Issue	Details	Raiser, Implementer	Completed
1.0.0	First release.	KWAN-TEK©	2024-01-29

PARTIAL

## 2. Introduction

### 2.1. NV centres in diamonds

The Nitrogen-Vacancy (NV) defect is one of the many coloured centres in diamond. Within the carbon crystal lattice, it consists of a substituted nitrogen atom directly adjacent to an atomic vacancy [Figure 2\(a\)](#). The NV centre can be considered as an artificial atom *trapped* within the diamond: its presence introduces energy levels within the diamond's wide band gap (5.5 eV), between which optical transitions are observed, like schematized in [Figure 2\(b\)](#). The corresponding *atomic* optical transition, called the Zero-Phonon Line (ZPL), has a wavelength of 637 nm. Due to the interaction of the NV centre with the diamond crystal lattice, this transition is actually greatly broadened. As a result, the peak of the absorption spectrum of the NV centre is shifted into the green, around 550 nm, while the emission maximum is centred in the red part of the visible spectrum, around 700 nm. In the end, both lines are almost 200 nm wide like depicted in [Figure 2\(c\)](#).

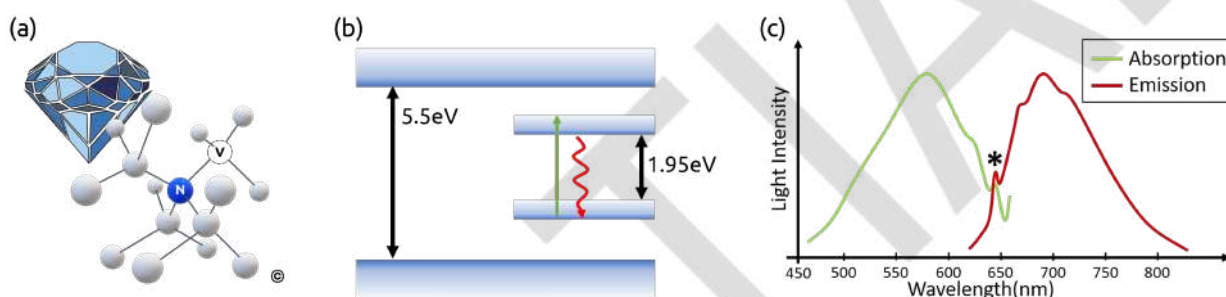


*Figure 2. The NV centre of diamond. (a) Schematic representation of the NV centre, composed of a nitrogen atom (N) juxtaposed with a vacancy (V). (b) Energy levels in diamond. Diamond is a wide band gap semiconductor. The presence of an NV centre induces sub-levels in the band gap, separated by ~ 1.95 eV. (c) Spectrum of optical transitions observed in the presence of NV centres. The green curve describes absorption and the red curve emission.*

Although NV centres naturally exist in diamond, their introduction into diamond can be controlled, in order to ensure a good purity of the diamond and satisfying density of NV centres. See for example [\[1\]](#) [\[2\]](#) to read further on the topic of diamond growth.

The NV centre exists in different charge states depending on the position of the Fermi level. However, we will only be interested in its negatively charged form,  $NV^-$ , which exhibits the spin manipulation properties that will study. In the remainder of this document, we will hence refer to the negatively charged NV centre as the NV centre.

### 2.2. NV centre orientation

The NV centre of diamond has a ( $C_{3v}$ ) crystalline symmetry, around the natural axis of symmetry that joins the nitrogen atom to the vacancy. The diamond crystal structure imposes four possible orientations for this axis within the lattice, corresponding to the four possible positions of the vacancy relative to a fixed nitrogen atom, as schematized in [Figure 3\(a\)](#).



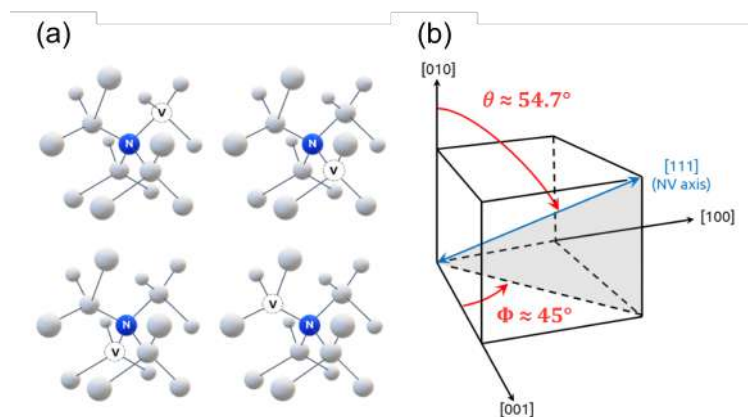


Figure 3. (a) The four possible orientations for the NV centre, corresponding to the four positions of the vacancy relative to the nitrogen. (b) Orientation of the  $[111]$  NV axis relative to the crystal orientations. In general, diamonds are cut along  $\{100\}$  planes.

The possible directions for the NV centres correspond to the diagonals of the diamond cubic matrix, i.e. the crystallographic axes  $\langle 111 \rangle$ . In the majority of parallelepipedic artificial diamonds, the facets are cut along  $\{100\}$  planes. The NV centres are therefore oriented with angles  $\theta = \arctan(\sqrt{2}) \approx 54.7^\circ$  and  $\phi = 45^\circ$  shown in Figure 3(b).

### 2.3. Spin properties

As shown in Figure 4, the dynamics of the NV centre can be described by a seven-level system.

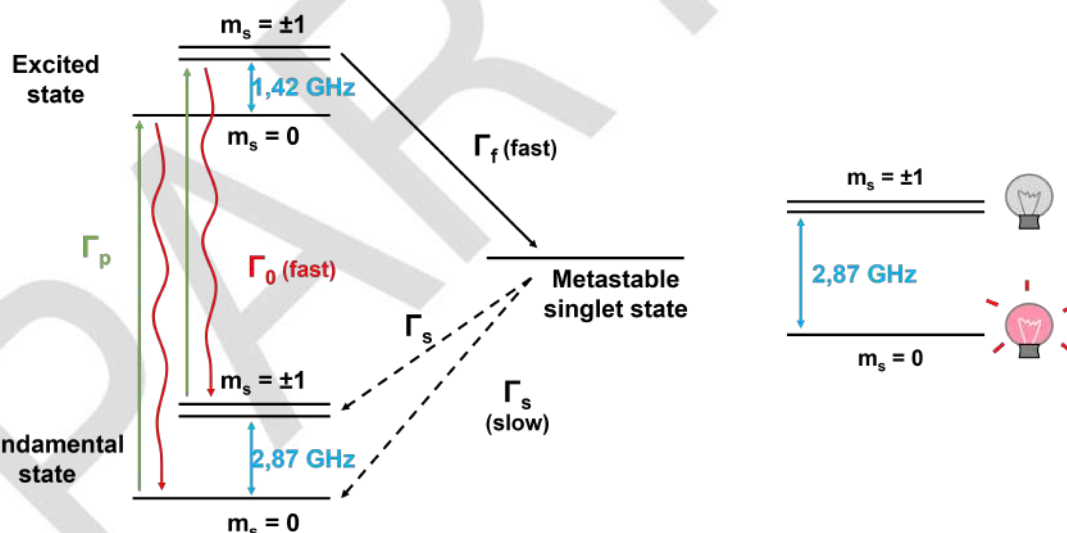


Figure 4. 7-level model of the NV centre (left) and its simplified version (right)

Because of the electronic structure of the defect, the NV centre has an overall electron spin  $S = 1$  (more details on the electronic structure of NV centre can be found for instance in [3]). The ground and excited states are therefore electron spin triplets, characterised by the quantum number  $m_s$ , which can take on the values 0,  $-1$  or  $+1$  depending on the projection of the spin along the quantisation axis. Because of the symmetry of the NV centre, the natural quantisation axis is the N-V axis, as mentioned earlier. The degeneracy between the  $|m_s = \pm 1\rangle$  and  $|m_s = 0\rangle$  states is partially lifted by the spin-spin interaction. The  $|m_s = \pm 1\rangle$

the ground and excited triplets, singlet metastable states exist in between. However their dynamics can readily be simplified to a single level, without impinging on the physical understanding of the system.

The optical transitions between the ground and excited states are spin conserving: they are represented in [Figure 4](#) by green arrows for laser excitation, and red ones for the photoluminescence. The rates  $\Gamma_P$  and  $\Gamma_0$  respectively describe the laser-induced pumping rate, proportional to the laser intensity, and the rate of spontaneous emission from the excited state. They are expressed in  $s^{-1}$  (see [Table 2](#)).

*Table 2. Summary of notations and values*

Notation	Description	Unit	Value
$\gamma$	Electronic gyromagnetic ratio of the ground state	Hz/T	$\sim 28 \times 10^9$
$\sigma_{NV}$	Optical absorption cross section	$m^2$	$3.1 \times 10^{-21}$
$\Gamma_P = \frac{\sigma_{NV} I_{opt}}{h\nu}$	Optical pumping rate	$s^{-1}$	$2.5 \times 10^4$ for laser intensity $I_{opt} = 2 \times 10^6 W \cdot m^{-2}$
$\Gamma_S$	Decay rate of the metastable state	$s^{-1}$	$5 \times 10^6$
$\gamma_1 = 1/T_1$	Population decay rate (return to thermal equilibrium)	$s^{-1}$	$\sim 10^3$
$\gamma_2 = 1/T_2$	Quantum coherence decay rate	$s^{-1}$	$\sim 5 \times 10^3$
$\Gamma_0$	Spontaneous emission rate	$s^{-1}$	$7 \times 10^7$
$\Gamma_f$	Decay rate from excited state $m_s = \pm 1$ to metastable state	$s^{-1}$	$5 \times 10^7$

The unique spin properties of the NV centre arise from the presence of the metastable state, strongly coupled to the excited  $|m_s = \pm 1\rangle$  states. While an NV centre in the  $|m_s = 0\rangle$  state will tend to cycle between the excited and ground states, an NV centre in the  $|m_s = \pm 1\rangle$  excited state has a non-negligible probability of decaying into the metastable state, without emitting a red photon. When in the metastable state, the NV centre can return to the ground state with a random spin projection (intersystem crossing). The decay rate  $\Gamma_f$  from the excited state  $|m_s = \pm 1\rangle$  into the metastable state is comparable to  $\Gamma_0$ . Under green light excitation, the NV centre therefore exhibits two important properties:

- the NV centre polarises in the  $|m_s = 0\rangle$  state;
- the  $|m_s = 0\rangle$  state emits more light than the  $|m_s = \pm 1\rangle$  states.

### 2.3.1. Hamiltonian operator of NV centre

Let us now consider that the NV centre is subjected to a magnetic field  $\mathbf{B}$  (see Figure 5).

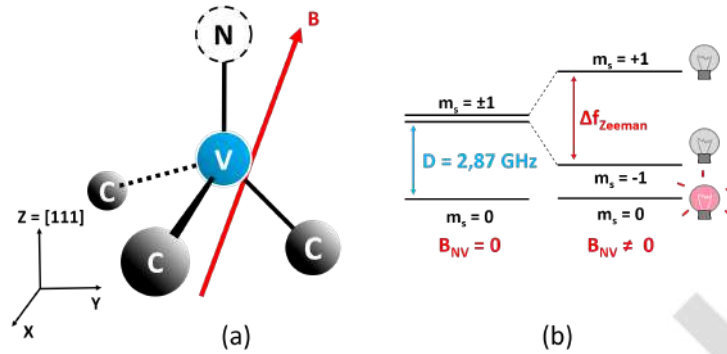


Figure 5. (a) NV centre with its vacancy (V), the nitrogen atom (N) and the 3 carbon atoms (C). (b) Lifting of the degeneracy of the  $|m_s = \pm 1\rangle$  states under the effect of a magnetic field (Zeeman effect).

In the  $(X, Y, Z)$  basis associated with the NV centre, with the Z axis coincident with that of the nitrogen-vacancy, it is possible to write the Hamiltonian of the ground state in the following form :

$$\mathcal{H} = \hbar D S_Z^2 + \hbar E (S_X^2 - S_Y^2) + g_{NV} \mu_B \mathbf{B} \cdot \mathbf{S} \quad (1)$$

With  $\hbar$  the Planck constant,  $\mu_B$  the Bohr magneton and  $g_{NV} \approx 2$  the Landé factor associated with the spin of the NV centre [3].  $S_X$ ,  $S_Y$  and  $S_Z$  are the Pauli spin matrices in the  $(X, Y, Z)$  basis, with  $\mathbf{S}$  the spin operator, and  $\mathbf{B}$  the vector of the applied magnetic field.  $D = 2.87$  GHz and  $E$  (typically between 100 kHz and 1 MHz in a bulk diamond) are the zero field splitting parameters. The first is due to the spin-spin interaction of the electrons in the NV centre, while the second describes the electric field and shear strain induced by imperfections in the diamond carbon lattice.

### 2.3.2. Zeeman effect

In general conditions, the three  $|m_s = 0, \pm 1\rangle$  states are not eistates of the system because  $S_X$  and  $S_Y$  do not commute with  $S_Z$ . However, one can easily find the eigenstates and eigenenergies of the system using appropriate approximations. For instance, the most common case encountered when using NV centres for their magnetic properties is when the magnetic field is strong enough so that the Zeeman term is stronger than the strain term, and applied along the NV symmetry axis (namely  $g_{NV} \mu_B B_Z > \hbar E$ ). In that case, one can write the Hamiltonian of the system to be:

$$\mathcal{H} = \hbar D S_Z^2 + g_{NV} \mu_B B_Z S_Z$$

(2)

It is easy to see that the three  $|m_s = 0, \pm 1\rangle$  states are then the eigenstates of the system with energies  $0, h(D \pm g_{NV}\mu_B B_Z)$ , as shown in Figure 5(b). This is the usual Zeeman effect one expects in a free atom for instance. A more comprehensive study on the resolution of the hamiltonian in various situations can be found for example in [4].

### 2.3.3. Hyperfine structure

In addition to the electronic spin properties mentioned, one needs to consider the interaction between the electrons and the nuclei of the system, and especially the nitrogen nucleus (for a comprehensive study of hyperfine interactions, one should also consider potential  $^{13}\text{C}$  nuclei around the NV centres). We will not dive into the details of this interaction, but simply state its main impact on the system. For a nuclear spin  $I$  of the nitrogen nucleus, each previously mentioned level ( $|m_s = 0, \pm 1\rangle$  of the ground state for instance) is split into  $2I + 1$  levels. The splittings between these  $2I + 1$  levels have a very small dependence with the magnetic field, so that they are generally considered constant.

In a magnetic resonance experiment, this effect results in going from one resonance line for each  $\Delta m_s = \pm 1$  transition to  $2I + 1$  around the same barycenter. The splitting ( $A_{hf}$ ) between these hyperfine lines only depends on the nitrogen isotope of the centre, ( $A_{hf} = 2.16\text{MHz}$ ) and  $3.05\text{MHz}$  respectively for  $^{14}\text{N}$  and  $^{15}\text{N}$ . Since  $^{14}\text{N}$  represents 99.64% of naturally occurring nitrogen, most NV centres in diamond are composed of this isotope (except for diamonds intentionally grown with  $^{15}\text{N}$ ). Figure 6(a) and (b) respectively represent the evolution of the ground state energy levels when considering the Zeeman and hyperfine interactions, and a typical resonance signal for  $^{14}\text{N}$ .

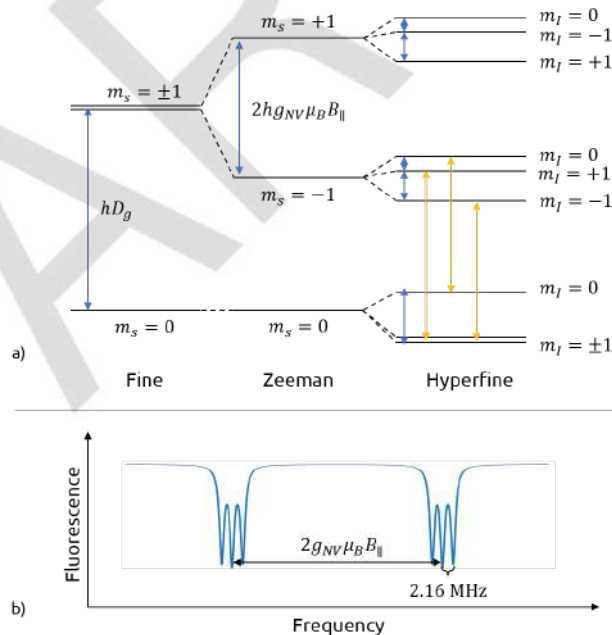


Figure 6. (a) NV ground state configuration for  $^{14}\text{N}$ . (b) Magnetic resonance signal for a magnetic field applied along the NV axis.

Also note that two very weak transitions may also appear on both sides of the main resonance, due to the interaction with the  $^{13}\text{C}$  nuclei inside the diamond. To go further on this topic, a comprehensive study of hyperfine interactions may be found for example in [3].

## 2.4. Optical bench

Figure 7 shows the whole set-up of KWANTEACH®, including the extension for pulsed measurement. It is an example of set up you can use for NV centres experiments.

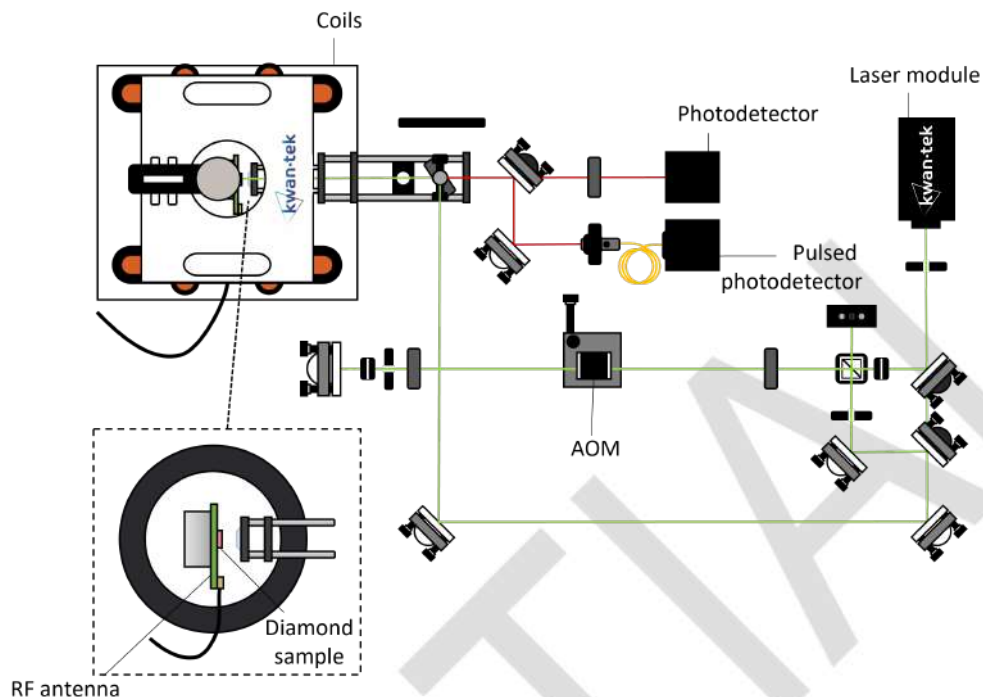


Figure 7. Optical bench for NV center experiments

In the Base module, a green laser beam is emitted by the laser module and directed towards the diamond sample fixed on a radio-frequency (RF) antenna, located at the centre of the coils. NV centres photoluminescence is collected and focused on a photodetector. The set-up is more detailed in [Base module: setting up and alignment](#).

In the extension Pulsed module, an Acousto-Optic Modulator (AOM) mounted in double-pass mode with a quarter-wave plate is added to establish the pulsed regime required for spin manipulation, as well as a specific photodetector. Flip mirrors enable to switch for Base to Pulsed set-up. The set-up is more detailed in [Pulsed module: setting up and alignment](#).

## 2.5. Spin manipulation

The aim of this kit of practical exercises is to familiarise students with fundamental concepts of quantum mechanics, such as  $T_1$  and  $T_2$  relaxation times, Rabi oscillations and quantum measurements. These concepts can be approached under simple experimental conditions, without vacuum or temperature control, through a series of experiments manipulating the electron spin of the NV centre [5]. All the manipulations will be carried out using software with a user interface allowing control of the parameters of interest.

### 2.5.1. Necessity of optical pumping

In order to extract enough signal from the spin states of the NV centres, it is of primary importance to ensure that a maximum of NV centres are put in the same state at the same time. Indeed, when looking for spin information, the overall signal is proportional to the population difference between the

interrogated levels. At thermal equilibrium, the occupation ratios  $n_i$  of the three spin states are governed by Boltzmann statistics, so that:

$$\frac{n_1}{n_0} \approx \frac{n_{-1}}{n_0} \approx \exp\left(\frac{-hD}{k_B T}\right) \approx 0.99954 \quad (3)$$

with  $k_B$  the Boltzmann constant and  $T$  the temperature (here 300 K).

Each state is hence equally populated by one third of the NV centres and no signal (or a signal with null contrast) can be extracted from the system. It is then essential to put the system out of equilibrium, which is done using optical pumping into the  $|m_s = 0\rangle$  state, taking advantage of the spin properties of NV centres (cf. [Spin properties](#)).

### 2.5.2. Optically detected magnetic resonance (ODMR)

Using also the property of brightness contrast between the states, the reading of the spin state can be done by measuring the photoluminescence signal. Once the NV centres are polarised, applying a resonant radio frequency excitation with the  $|m_s = 0\rangle \leftrightarrow |m_s \pm 1\rangle$  transition, a population transfer between the two spin states will lead to a drop in the photoluminescence signal, as observed in [Figure 8](#).

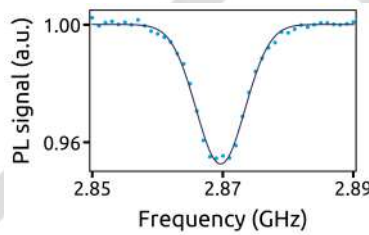


*Figure 8. Magnetic resonance spectrum in zero field; the solid line is a Gaussian fit of the data.*

In the presence of a magnetic field with a strong component ( $B_{//}$ ) along the quantization axis of the NV centre, the degeneracy of the  $|m_s = \pm 1\rangle$  states is lifted, by the Zeeman effect (cf [Zeeman effect](#)). The separation between the  $|m_s = +1\rangle$  and  $|m_s = -1\rangle$  states is equal to  $hg_{NV}\mu_B B_{//}$ , making the NV centre an atomic scale magnetometer. In [Figure 9](#), 8 lines can be observed in the magnetic resonance spectrum, which correspond to the four  $|m_s = 0\rangle \leftrightarrow |m_s = \pm 1\rangle$  transitions in the four  $\langle 111 \rangle$  crystal orientations of diamond.

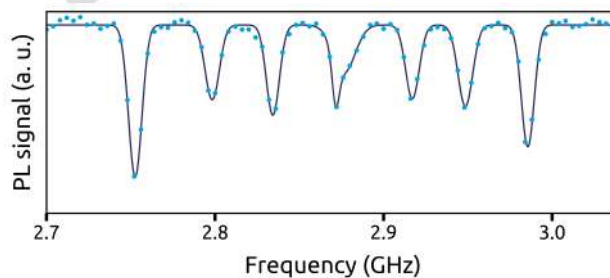


*Figure 9. Magnetic resonance spectrum under the application of a bias field of a few mT. The 8 lines correspond to the two transitions between the states  $|m_s = 0\rangle \leftrightarrow |m_s = -1\rangle$  and  $|m_s = 0\rangle \leftrightarrow |m_s = +1\rangle$  of each of the four crystal orientations.*



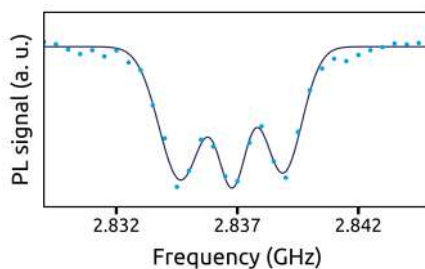


Figure 10. Typical hyperfine structure of the NV centre.

### 2.5.3. Longitudinal relaxation time $T_1$

The longitudinal relaxation time, or  $T_1$ , is the time required for the system to return into thermodynamic equilibrium once it has been polarised to its  $|m_s = 0\rangle$  spin state.

The standard  $T_1$  measurement sequence is shown in Figure 11. It consists of a first initialisation laser pulse, in order to polarise the system into the  $|m_s = 0\rangle$  spin state, followed by a free evolution time, in the dark, of variable duration  $\tau$ . The last step is a readout laser pulse, which extracts the spin state of the NV centre via the photoluminescence signal.

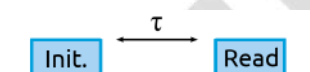


Figure 11. Standard  $T_1$  relaxation time measurement sequence, consisting of two laser pulses.

Figure 12 shows the evolution of the photoluminescence signal as a function of the free evolution time  $\tau$  in the dark. For short durations  $\tau$ , the system does not have time to return to its thermodynamic equilibrium. It remains polarised in its  $|m_s = 0\rangle$  spin state, which results in a high photoluminescence signal. The gradual relaxation of the system towards its thermodynamic equilibrium results in the fall in photoluminescence for longer times  $\tau$ .

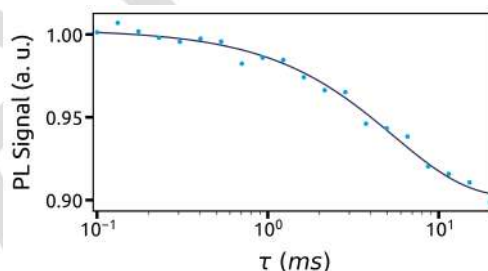


Figure 12. Measuring the time  $T_1$  on a set of NV centres hosted in a bulk diamond. The solid line is a fit by an exponential decay.

Fitting the data by an exponential decay allows us to extract the longitudinal relaxation time  $T_1 = 5.4 \pm 0.5$  ms, which is typical of an NV centres ensemble in a bulk diamond. The  $T_1$  time is limited by the interactions between the NV centre and the phonons in the crystal lattice [6].

### 2.5.4. Coherent control of spin state: Rabi oscillations

In the following, a bias magnetic field of a few mT will be applied along the quantization axis of the NV centre, in order to lift the degeneracy between the  $|m_s = \pm 1\rangle$  states. Applying a resonant radio-frequency wave with one specific transition, we can consider the

Coherent control of the spin state of an NV centre can be achieved by performing Rabi oscillations between the  $|m_s = 0\rangle$  and  $|m_s = +1\rangle$  states [7]. The sequence used is shown in Figure 13.

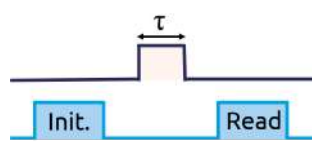


Figure 13. Typical Rabi oscillation measurement sequence

It consists of a first initialization laser pulse, which polarizes the NV centre into its  $|m_s = 0\rangle$  spin state. This is followed by a radio-frequency pulse of variable duration  $\tau$ , resonant with the transition  $|m_s = 0\rangle \leftrightarrow |m_s = +1\rangle$ : this is the manipulation step. The spin state after this step is a superposition of state  $\alpha|m_s = 0\rangle + \beta|m_s = +1\rangle$ . The spin state of the system is then extracted by a final readout laser pulse. The Bloch sphere representation of each step is shown in Figure 14.

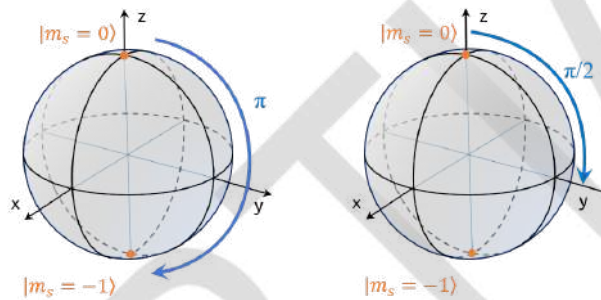


Figure 14. Representation on the Bloch sphere of the spin of the system (red arrow) at each stage

A typical Rabi oscillation signal is shown in Figure 15. For very short microwave pulse durations, the populations do not have time to switch from the  $|m_s = 0\rangle$  state to the  $|m_s = +1\rangle$  state, the photoluminescence signal remains maximum. For a radio frequency pulse duration  $T_\pi$ , a population maximum of the  $|m_s = 0\rangle$  state has switched to the  $|m_s = +1\rangle$  state, so the photoluminescence signal is minimum. The coherent oscillations between these two states are represented by the oscillations of the photoluminescence signal. These Rabi oscillations allow us to define the times  $T_\pi$  and  $T_{\pi/2}$ , which are at the heart of the spin dynamics sequences.



Figure 15. Typical Rabi oscillations measured on an NV centre ensemble hosted in a bulk diamond. The solid line is a fit by a sinusoidal function with an exponential decay envelope.

### 2.5.5. Dephasing time $T_2^*$

Dephasing is randomization of the phase between the states of an ensemble where all its compounds are initially set in a quantum superposition such as  $|\psi\rangle = \frac{1}{\sqrt{2}}|m_s = 0\rangle + \frac{1}{\sqrt{2}}|m_s = +1\rangle$ .

This phenomenon is characterised by the dephasing time  $T_2^*$ . It can be measured by the Ramsey fringe method. The sequence is shown in Figure 16. After pumping, the manipulation step consists of a first radio frequency pulse of duration  $T_{\pi/2}$  to set the system in a superposition state, as described by the equation above.

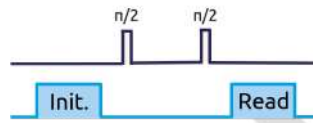


Figure 16. Ramsey fringe measurement sequence

The system then freely evolves for a time  $\tau$ , through free precession. Each NV centre accumulates a phase, which depends on its environment and in particular on the magnetic fluctuations of the spin bath. Finally, a second radio-frequency pulse of duration  $T_{\pi/2}$ , followed by the readout laser pulse allows the spin state of the system to be read out. This spin state manipulation step is shown on the Bloch sphere in Figure 17.

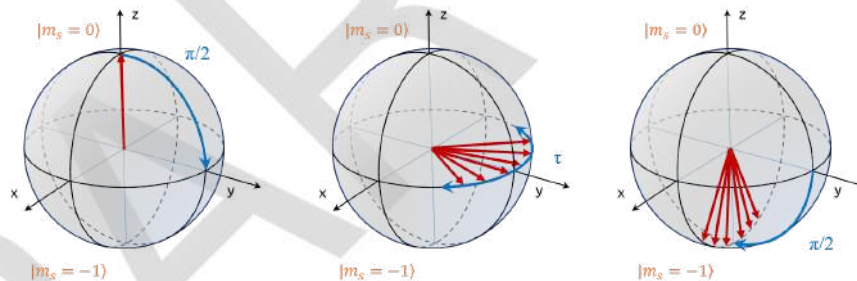


Figure 17. Representation on the Bloch sphere of the spin state during the manipulation step for the Ramsey fringe method

A typical Ramsey fringe measurement is plotted in Figure 18. The decay of the oscillations corresponds to the dephasing time, which can be extracted by fitting these data [8][9], to give  $T_2^* = 456 \pm 45$  ns. The dephasing of the NV centres is governed by the interactions with the spin bath, composed of [8]:

- Nuclear spins, such as  $^{13}\text{C}$  atoms [8], with a natural abundance of 1.1% and a nuclear spin  $I = 1$
- Electronic spins, such as nitrogen impurities [9]
- Electron spins on the surface of diamond [4]

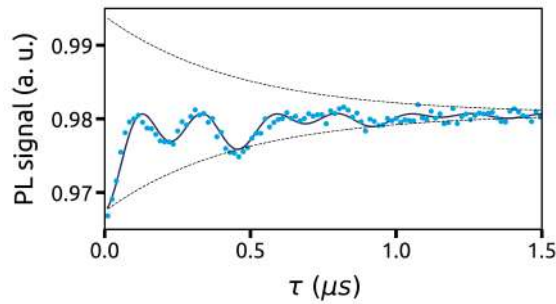


Figure 18. Ramsey fringe measurement on a set of NV centres. The  $T_2^*$  coherence time is extracted by a fit described in reference [8].

It is possible to reduce the impact of the environment when isolating the system from the magnetic noise generated by the surrounding spin bath. In that case, we refer to the characteristic time as the coherence time instead of dephasing time, noted  $T_2$ .

### 2.5.6. Dynamic decoupling: coherence time $T_2^{echo}$

The simplest dynamic decoupling sequence to implement is the Hahn echo sequence [10]. As schematised in Figure 19, the handling phase is similar to that presented above for the  $T_2^*$  time measurement, except that a radio frequency pulse of duration  $T_\pi$  is applied in the middle of the free precession time.

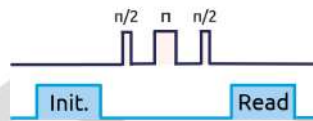
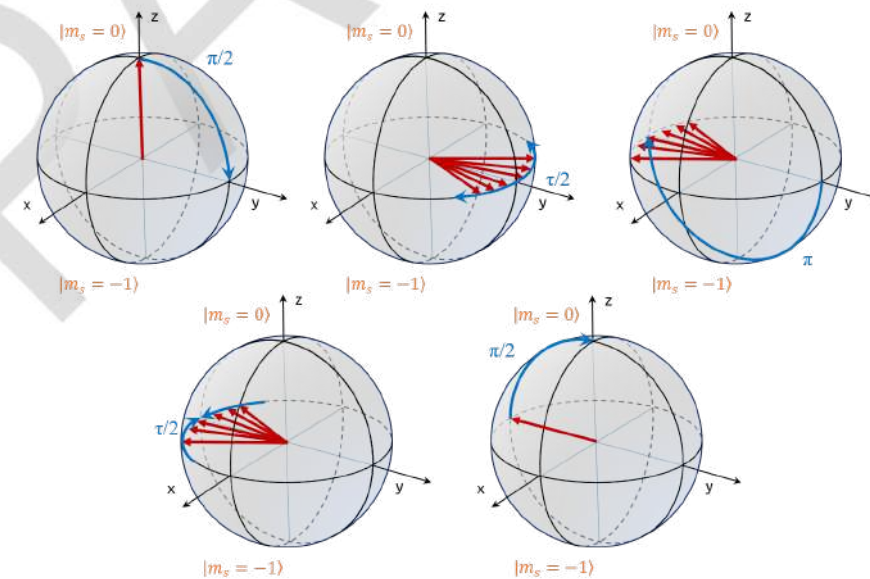


Figure 19. Hahn echo sequence

The accumulated phase shift during the time  $\tau/2$  is thus compensated by the accumulated phase during the second free precession time  $\tau/2$ , as shown on the Bloch sphere in Figure 20. This method rejects the slow fluctuations of the environment (such as the spin bath), thus "isolating" the NV centres from the environment.



*Figure 20. Representation on the Bloch sphere of the spin state during the manipulation step for a Hahn echo sequence*

A typical  $T_2^{echo}$  time measurement is plotted in Figure 21. Fitting the data reveals a  $T_2^{echo}$  coherence time of  $3.8 \pm 0.2 \mu\text{s}$ .

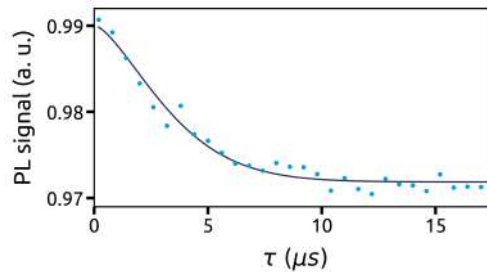


*Figure 21. Measurement of  $T_2^{echo}$  coherence time. The data is fitted by an exponential decay to the power of 2.*

## References

- [1] Tallaire, A. et al. High NV density in a pink CVD diamond grown with N<sub>2</sub>O addition. Carbon 170, 421-429 (2020).
- [2] Achard, J., Jacques, V. & Tallaire, A. Chemical vapour deposition diamond single crystals with nitrogen-vacancy centres: a review of material synthesis and technology for quantum sensing applications. J. Phys. D: Appl. Phys. 53, 313001 (2020).
- [3] M. W. Doherty, F. Dolde, H. Fedder, F. Jelezko, J. Wrachtrup, N. B. Manson, and L. C. L. Hollenberg, Theory of the Ground State Spin of the NV<sup>-</sup> Center in Diamond: I. Fine Structure, Hyperfine Structure, and Interactions with Electric, Magnetic and Strain Fields, Phys. Rev. B 85, 205203 (2012).
- [4] L. Rondin et al., Surface-Induced Charge State Conversion of Nitrogen-Vacancy Defects in Nanodiamonds, Phys. Rev. B 82, 115449 (2010).
- [5] Y. Yang, H. H. Vallabhapurapu, V. K. Sewani, M. Isarov, H. R. Firdausy, C. Adambukulam, B. C. Johnson, J. J. Pla, and A. Laucht, Observing Hyperfine Interactions of NV<sup>-</sup> Centers in Diamond in an Advanced Quantum Teaching Lab, American Journal of Physics 90, 550 (2022).
- [6] A. Jarmola, V. M. Acosta, K. Jensen, S. Chemerisov, and D. Budker, Temperature- and Magnetic-Field-Dependent Longitudinal Spin Relaxation in Nitrogen-Vacancy Ensembles in Diamond, Phys. Rev. Lett. 108, 197601 (2012).
- [7] F. Jelezko, T. Gaebel, I. Popa, A. Gruber, and J. Wrachtrup, Observation of Coherent Oscillations in a Single Electron Spin, Phys. Rev. Lett. 92, 076401 (2004).
- [8] J. R. Maze, A. Dréau, V. Waselowski, H. Duarte, J.-F. Roch, and V. Jacques, Free Induction Decay of Single Spins in Diamond, New J. Phys. 14, 103041 (2012).



[9] E. Bauch et al., Decoherence of Ensembles of Nitrogen-Vacancy Centers in Diamond, Phys. Rev. B 102, 134210 (2020).

[10] E. L. Hahn, Nuclear Induction Due to Free Larmor Precession, Phys. Rev. 77, 297 (1950).

PARTIAL

## 3. Base module: setting up and alignment

### 3.1. General installation

This section describes the general configuration of KWANTEACH® Base, as illustrated in Figure 22. This configuration of the parts on the breadboard is the one we propose. You can modify it if it seems relevant to you.

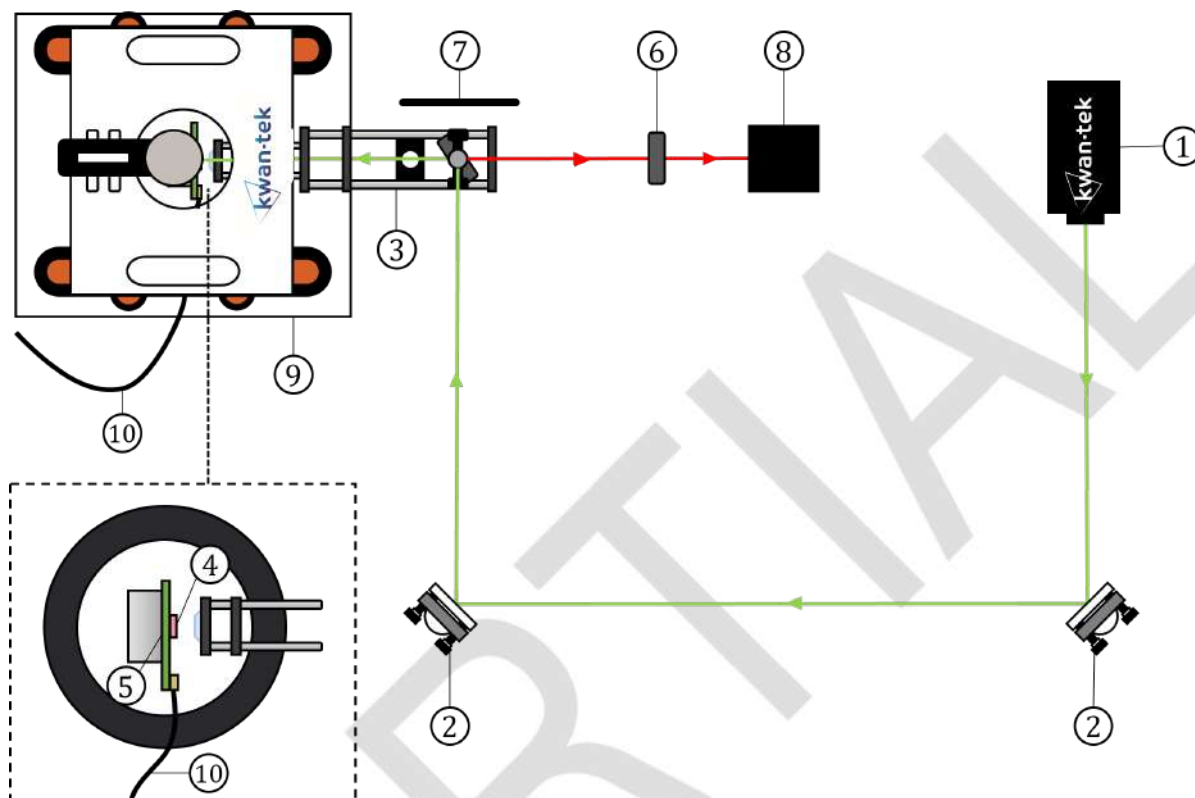


Figure 22. Set-up diagram. ① laser module. ② fixed kinematic mirrors. ③ cage system. ④ diamond sample. ⑤ radio-frequency antenna. ⑥ converging lens. ⑦ laser safety screen. ⑧ photodetector. ⑨ coils. ⑩ power supply cable.

The laser module (①) emits a green laser beam at 532 nm, with a maximum power of 140 mW. This laser beam is reflected on two alignment mirrors (②). In the cage system (③), a dichroic mirror reflects the green beam towards the NV doped diamond sample (④). A small part of the incident laser light passes through the dichroic, thus a laser safety screen must be added to block it (⑦). The diamond is fixed on a radio-frequency (RF) antenna (⑤), located at the centre of the coils (⑨). In the cage, two iris diaphragms allow to align the laser beam on the centre of the aspheric lens which focuses the green light onto the diamond. NV photoluminescence is collected and collimated by the same aspheric lens. The red light is transmitted through the dichroic mirror. A coloured glass filter absorbs the residual green light from the laser. Finally, a converging lens (⑥) focuses the red light on the photodetector (⑧).

In the following, the mounting of separate parts, the assembling on the breadboard and the alignment procedure are detailed.

### 3.2. Mounting parts

### 3.2.1. Optical post mounting

To mount an optical post assembly, 3 parts are required (see [Figure 23](#)):

- a post base: *BE1/M*
- a post: *TR100/M* or *TR75/M*
- a post holder: *PH100/M* or *PH75/M*



*Figure 23. Optical post elements*

Follow the instructions below:

- Fix the post base to the post holder using a 3 mm Allen key as shown in [Figure 24](#).



*Figure 24. Base and post holder assembling*

- Insert the optical post into the post holder.



PARTIAL



PARTIAL





PARTIAL

### 3.2.2. Adjusting the focus of the laser beam in the diamond

To obtain a fluorescence signal, the laser beam from the aspherical lens must be focused inside the diamond (④).

- Check that the diamond is placed between the aspheric lens and its focal plane. The working distance of the aspheric lens is 7.46 mm.
- Check that the diamond is placed between the aspheric lens and its focal plane. The working distance of the aspheric lens is 7.46 mm.
- Make sure that the laser spot is located on the diamond. You can check the red photoluminescence light emitted by the diamond through the laser safety goggles.



Reminder: laser safety goggles must always be put on when manipulating KWANTEACH®.

- Place the white screen between the red filter and the converging lens (⑥), check that you are able to see some fluorescence light. To adjust the focus, loosen the cage adapter and move back slightly the 16 mm cage (see [Figure 32](#)) to bring the focal point of the aspheric lens closer to the centre of the diamond (see [\[aspherical\\_position\]](#)). The red spot on the white screen must be well defined and its optical power must be homogenous.

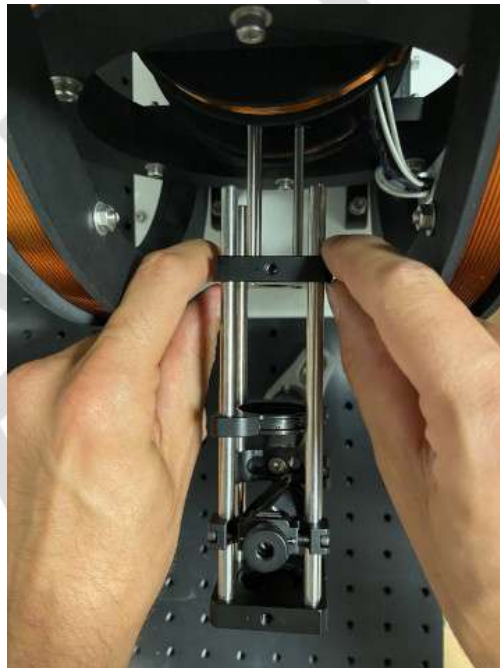


*Figure 32. Adjusting the focus of the laser beam in the diamond by translating the cage adapter*

- When the focus is done, fix the cage adapter.



PARTIAL

## 4. Optically Detected Magnetic Resonance (ODMR)

### 4.1. Theoretical principles

As presented in the introductory chapter, a continuous green light illumination pumps most of the NV centres in the  $|m_s = 0\rangle$  spin state of the fundamental state. A resonant radio frequency (RF) applied on the system can then induce atomic transitions between the  $|m_s = 0\rangle$  spin state and either  $|m_s = +1\rangle$  or  $|m_s = -1\rangle$  states. This magnetic resonance can be observed in several ways, one is through the level of red photoluminescence emitted by the NV centers. Since the  $|m_s = 0\rangle$  state is brighter than the two other states, the NV centers emit more photoluminescence from  $|m_s = 0\rangle$  than from  $|m_s = \pm 1\rangle$ . While performing a magnetic resonance experiment, the luminescence hence drops. Detecting the resonance using this drop is called an Optically Detected Magnetic Resonance (ODMR).

### 4.2. Experimental protocol

#### 4.2.1. ODMR acquisition with no external magnetic field

- Once the alignment is done and the DC level of the photoluminescence signal optimized, connect the antenna to the *RF OUT* port of the KWANTEACH® Base unit with an SMA cable. Make sure that the KWANTEACH® Base photodetector is supplied and that its signal output is connected to the *Photodetector signal* port of the control unit. You can also connect the *Trigger* output of the unit and the photodetector output to an oscilloscope.
- Open the *ODMR acquisition* tab of the KWANTEACH® software. Set the *Low frequency* and *High frequency* value so that the RF frequency ramp is centred on 2.87 GHz. Choose preferably a low RF power value (around 6 dBm) and a large number of points. *Average mode* is selected by default, user can set the number of acquisitions to average in the *Average* spinbox.



When using *Average mode* and set  $n$  average, the microwave output will generate  $n$  consecutive microwave frequency ramp and the user will observe the averaged signal.

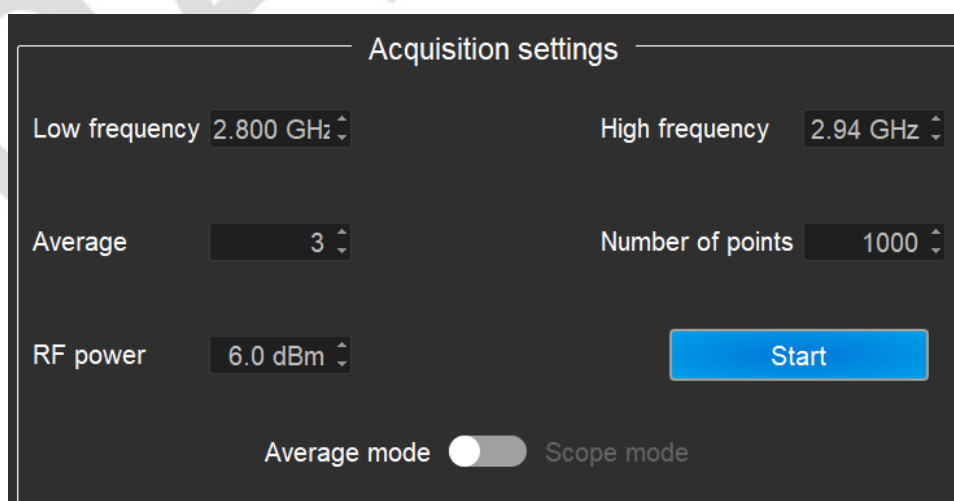


Figure 34. Screenshot of standard acquisition settings for ODMR acquisition

on the KWANTEACH® Base interface.



Make sure that the photodetector output voltage does not exceed 4 V. If this is the case, lower the laser power with the thumb-wheel on the unit.

#### 4.2.2. Interpretation of a zero-field ODMR spectrum

Figure 35 represents an ODMR signal with no external magnetic field. This signal is characterized by a drop in light power around the central frequency (2.87 GHz). This drop is due to the magnetic transitions between the  $|m_s = 0\rangle$  and the  $|m_s = \pm 1\rangle$  spin levels of the fundamental state.

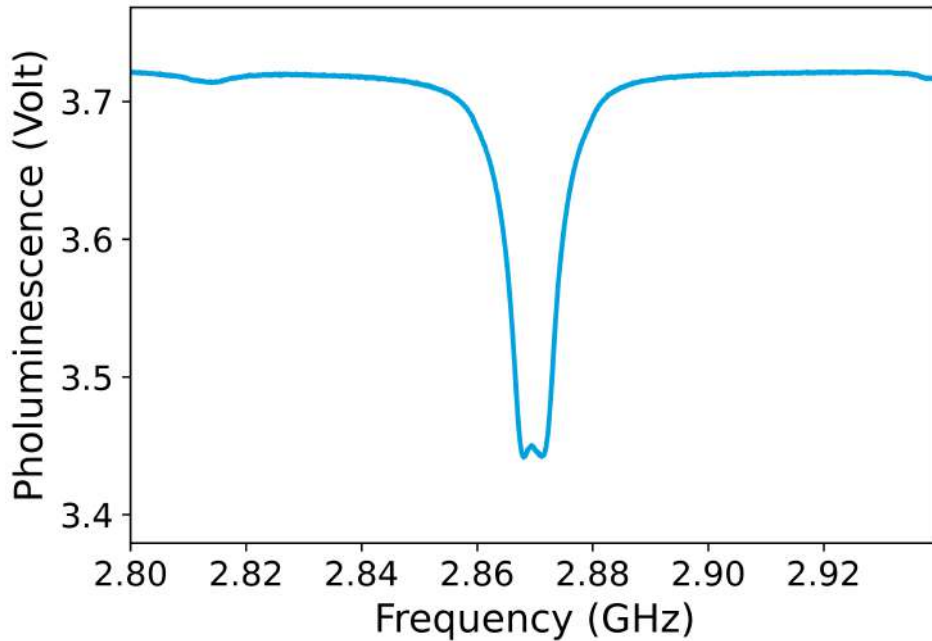


Figure 35. Zero-field ODMR spectrum acquired with standard parameters

In the absence of a magnetic field, a partial degeneracy lifting is observed in the signal, as can be seen in Figure 35. It is characterized by the two drops around the central frequency, and is due to mechanical strain at the atomic level. This strain is responsible for the  $S_X^2 - S_Y^2$  term in the NV centre Hamiltonian (see [Hamiltonian operator of NV centre](#)), and results at null field in two eigenstates  $\frac{1}{\sqrt{2}}(|m_s = +1\rangle + |m_s = -1\rangle)$  and  $\frac{i}{\sqrt{2}}(|m_s = +1\rangle - |m_s = -1\rangle)$ , separated from each other by an energy of  $2\hbar E$ , with  $\hbar$  the Planck constant and  $E$  a zero field splitting parameter.

## 5. Observation of the Zeeman effect at low field

### 5.1. Theoretical principles

When a magnetic field is applied on the NV centres, their spin states are shifted depending on their spin quantum number. For low fields, or as long as the direction of the field coincides with the symmetry axis of the NV centres (see [Figure 36](#)), the shifting is linear with the magnetic field. The proportionality factor is the gyromagnetic ratio, which is close for the NV electron spin to the one of a free electron spin. The Zeeman shifts are described by the following evolution of the resonance frequencies:

$$f_{\pm} = D_g \pm \sqrt{(\gamma \|\vec{\mathbf{B}}_{\parallel}\|)^2 + E^2} \quad (4)$$

with  $\gamma$  the NV gyromagnetic ratio,  $D_g$  the zero-field splitting and  $E$  the strain parameter. This expression can be simplified in the regime where the magnetic field  $\mathbf{B}$  is much greater than the strain parameter  $\gamma \|\vec{\mathbf{B}}_{\parallel}\|^2 \gg E^2$ . With the diamond provided, the strain parameter is of the order of  $E \sim 1$  MHz, which corresponds to magnetic fields larger than 0.5 mT. In such case, the Zeeman shifts can be simplified as follow:

$$f_{\pm} = D_g \pm \gamma \|\vec{\mathbf{B}}_{\parallel}\| \quad (5)$$

For higher fields, not perfectly aligned with the symmetry axis of the NV centres, the Zeeman shifts becomes non-linear (see for example reference [\[11\]](#)). The resonance frequencies can then be approximated by a power series. To second order in magnetic field, they are given by:

$$f_{\pm} = D_g \pm \gamma \|\vec{\mathbf{B}}_{\parallel}\| + \frac{3}{2} \frac{(\gamma \|\vec{\mathbf{B}}_{\perp}\|)^2}{D_g} \quad (6)$$

with  $\vec{\mathbf{B}}_{\parallel}$  the projection of the magnetic field along the NV symmetry axis,  $\vec{\mathbf{B}}_{\perp}$  its perpendicular projection (see [Figure 36](#)).

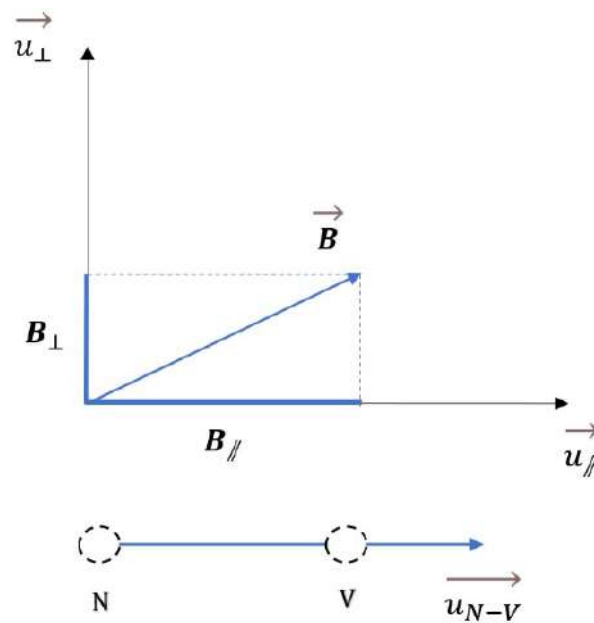


*Figure 36. Representation of the NV symmetry, showing perpendicular and parallel directions.*

In diamond, because of the crystallographic lattice, NV centres can be oriented along the four  $\langle 111 \rangle$  directions. There are thus four possible families of NV centres, having each two resonance frequencies. For this reason, in a diamond highly doped with NV centres, one can generally observe up to eight resonances in total in an optical detection of magnetic resonance (ODMR) experiment.



PARTIAL



By approaching a magnet close to the diamond, or applying a weak magnetic field on the coils, observe the splitting of the lines with the magnetic field. An ODMR can be obtained like the one shown in [Figure 39](#) (ODMR spectrum obtained). It can be seen that the ODMR contains more than two lines.

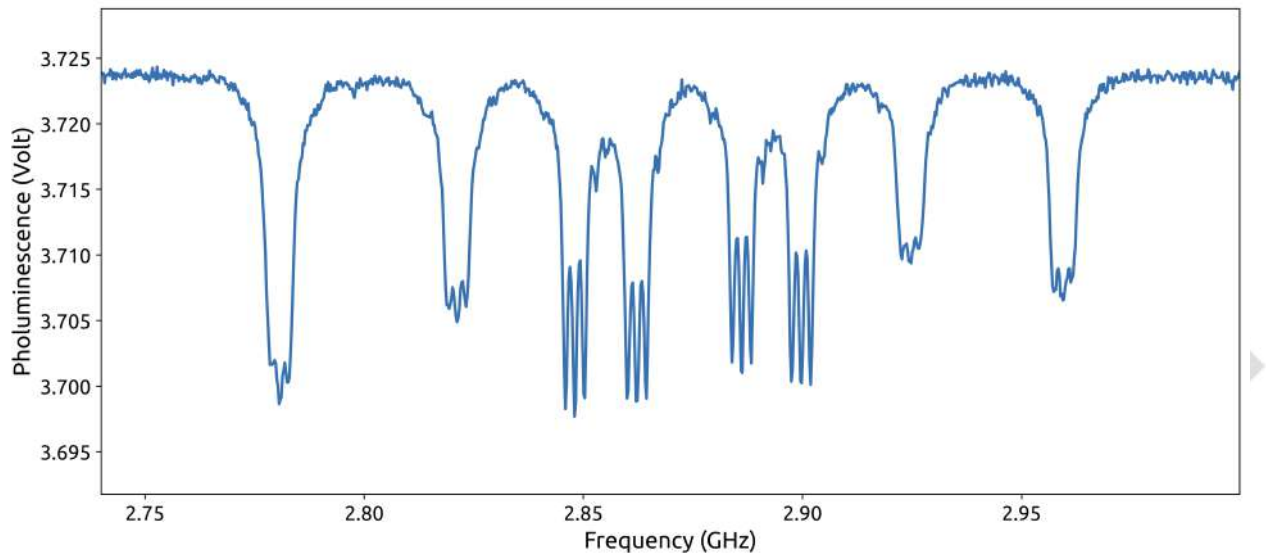


*Figure 39. ODMR spectrum obtained by approaching a Neodymium permanent magnet close to diamond*

- Vary the magnetic field (using the interface for the coils) to observe the splitting of the lines with the magnetic field.
- With the coils, rotate the field (with a constant norm) and check that the splitting maxima corresponds to the orientation of the  $\langle 111 \rangle$  crystallographic directions. For this splitting, the current values in the coils must be the same for each axis. A spectrum like the one of [Figure 40](#) should be obtained.
- Acquire an ODMR spectrum for one of these orientations.

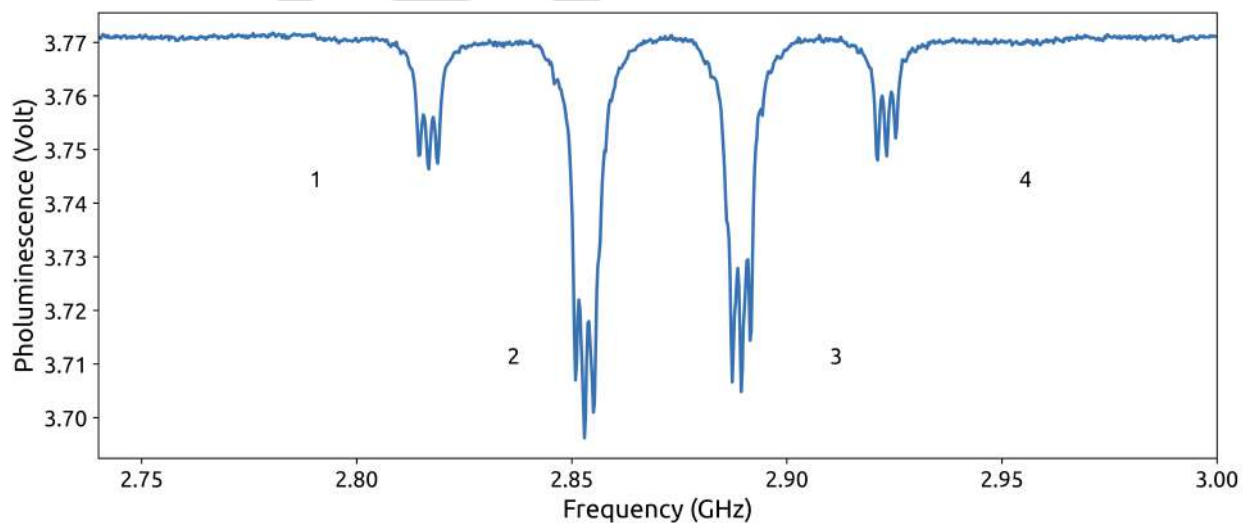


*Figure 40. ODMR spectrum for a field collinear with a large diagonal of the crystal lattice of the diamond*

By applying a magnetic field collinear with a  $\langle 111 \rangle$  direction of the crystal lattice of the diamond, the magnetic field is aligned with one of the 4 orientations of NV centres. In this case, the 3 other orientations see the same field projections. Thus, only 2 pairs of resonances can be observed. One pair close to 2.87 GHz with a strong contrast (denoted 2 and 3) and another pair further from the central frequency but with a weaker contrast (denoted 1 and 4). Lines 1 and 4 correspond to the NV orientation collinear with the magnetic field, while lines 2 and 3 correspond to the contribution of the 3 other orientations.

### 5.1.2. Characterization of the gyromagnetic ratio of the electron

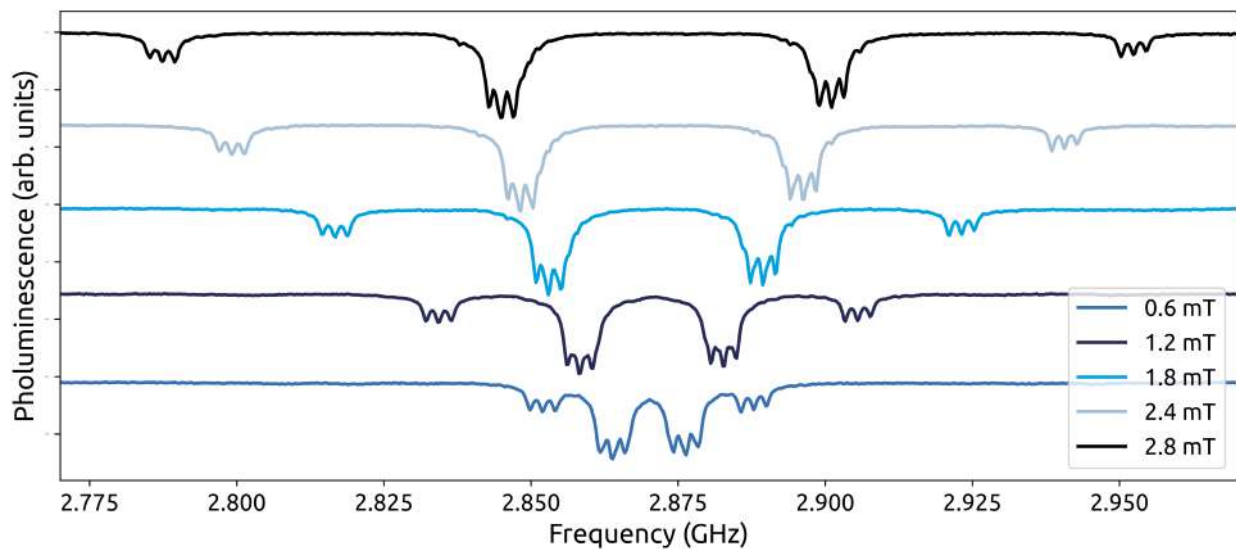
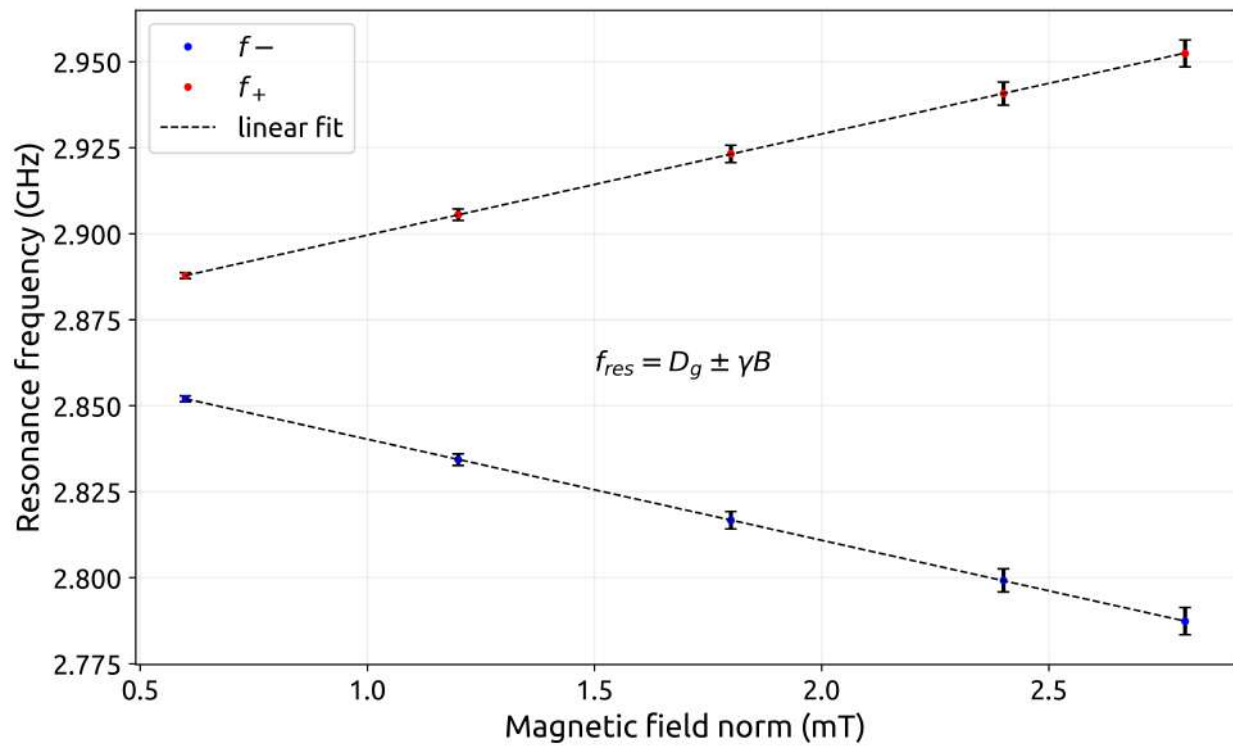


Figure 41. Splitting of ODMR lines according to the magnetic field norm



*Figure 43. Evolution of the ODMR lines frequencies as a function of the magnetic field. The field is applied along the NV centers axis. The blue and red markers correspond to the data taken for the lower and higher resonances respectively.*

### 5.1.3. Highlighting the nonlinear term of the Hamiltonian

In order to highlight the nonlinear evolution of the Zeeman effect in NV centres, it is necessary to apply a magnetic field with a strong perpendicular component  $B_{\perp}$ . To do this, a magnetic field is applied so that the 4 orientations see different field components.

After a series of seven acquisitions, a plot similar to Figure 45 can be obtained, where one can clearly see the effect of the quadratic term of Equation (6).

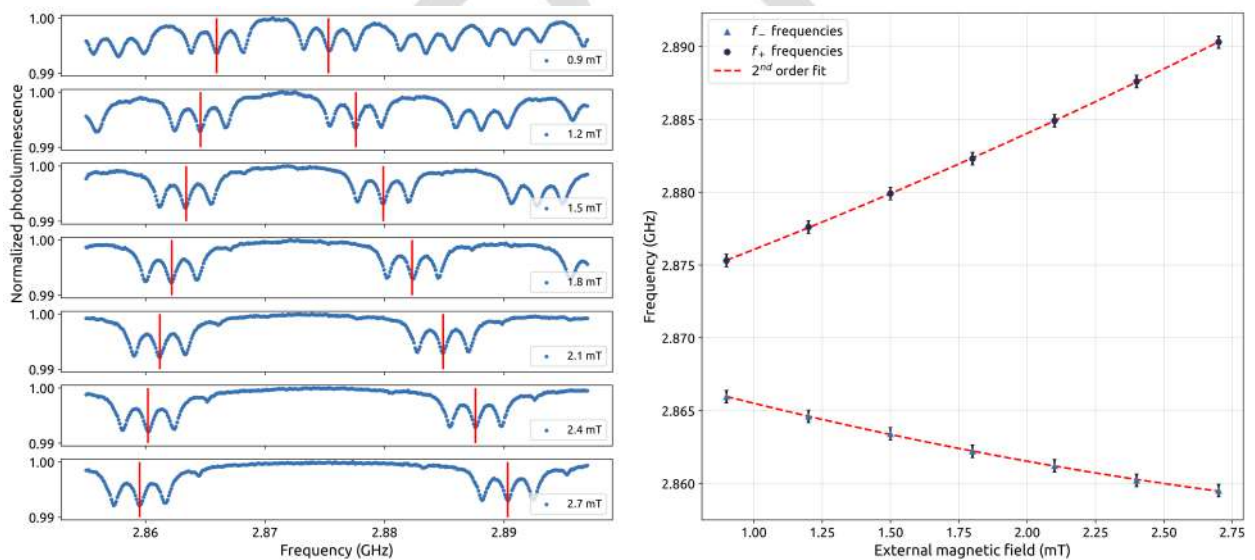


Figure 45. Resonance frequencies of an NV orientation with a strong perpendicular component as a function of the magnetic field norm.



PARTIAL



## 6. Observation of hyperfine lines

### 6.1. Theoretical principles

Like presented in the introduction chapter [Hyperfine structure](#), the coupling of the electron spin with the neighbouring nitrogen-14 atoms ( $^{14}\text{N}$ ) gives rise to a specific hyperfine structure. The hyperfine structure can be observed at low RF power, by zooming on one fine resonance line. This is easier for example when the eight resonance lines are split thanks to the Zeeman shifts.

PARTIAL



## 6.2. Experimental protocol

### 6.2.1. Hyperfine spectrum measurement

- To visualize the hyperfine lines, apply a magnetic field with the coils to isolate a fine line. For instance, apply a magnetic field allowing to split the eight ODMR lines to be sure about observing an isolated hyperfine line.



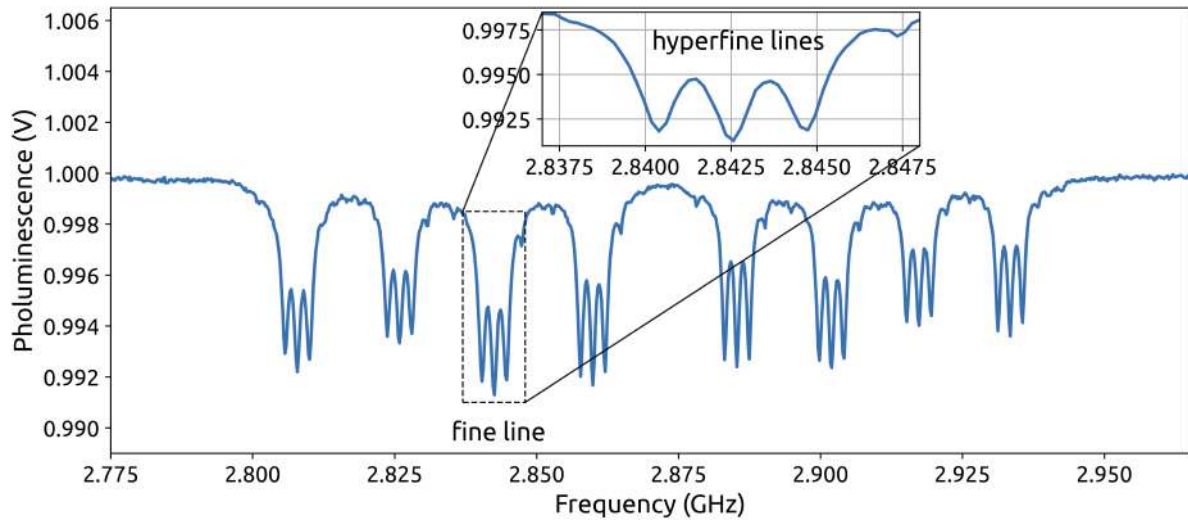


Figure 47. Zoom on fine lines to see the three hyperfine levels

### 6.2.2. Hyperfine splitting estimation

### 6.2.3. Influence of radio frequency power on hyperfine lines

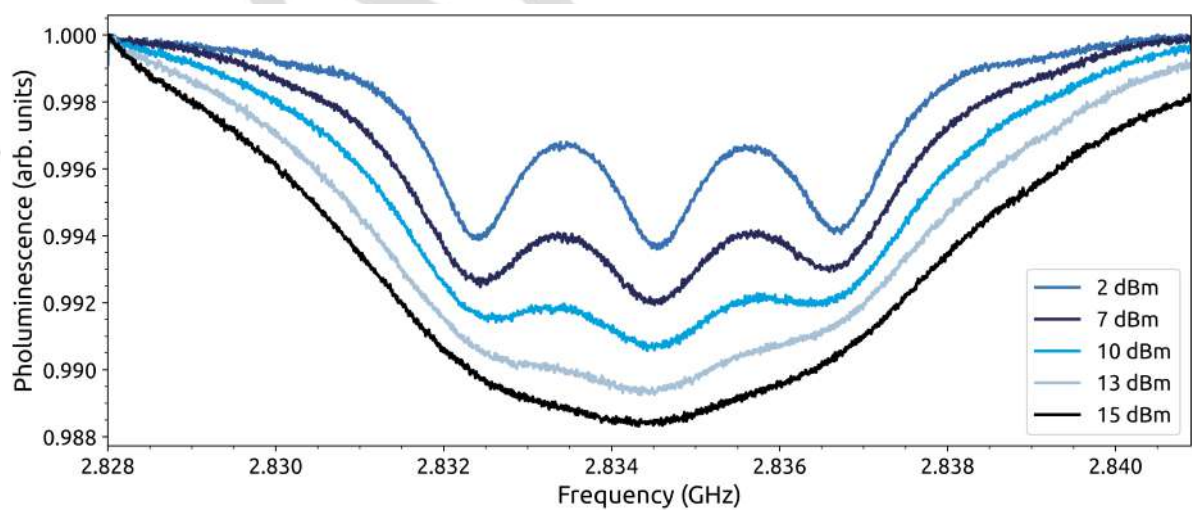


Figure 49. Impact of RF power on the width of hyperfine lines. To visualize this impact, a series of acquisitions of the same ODMR line is made for different microwave powers.

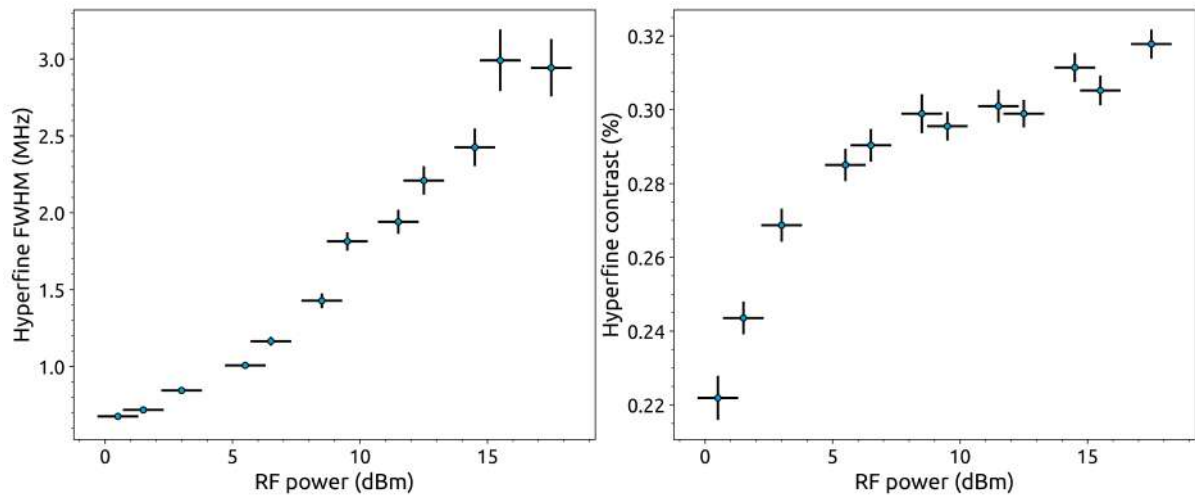


Figure 50. Right: evolution of the hyperfine lines FWHM with the RF power. Left: evolution of the contrast of the hyperfine lines with the RF power .



## 7. Earth field measurement

### 7.1. Theoretical principles

#### 7.1.1. Measurement of the orientation and norm of the Earth magnetic field

In this part we will provide an example of magnetic field measurement, by using the NV diamond as a magnetometer. The aim of this section is to show how to retrieve the orientation and norm of the Earth magnetic field.

PARTIAL



### 7.1.2. Magnetic field reconstruction

To reconstruct the Earth magnetic field from the two spectra, we first need to associate each ODMR line to its NV orientation. To do this, we have to calculate the projection of the field of the coil on each orientation.



PARTIAL

## 7.2. Experimental protocol

### 7.2.1. ODMR spectrum acquisition



PARTIAL



### 7.2.2. Definition and designation of crystal orientations on spectra

### 7.2.3. Determination of the ODMR frequencies and calculation of the Earth field





#### **7.2.4. Uncertainty of the measurement**

The uncertainty in measuring the components of the earth's magnetic field is directly linked to the uncertainty in the currents delivered in the coils.



From this, we can estimate the accuracy of the measurement of the Earth field:

$$\vec{B}_{Earth} = \begin{pmatrix} -13.73 \pm 1.89 \\ 0.59 \pm 0.94 \\ -46.81 \pm 5.96 \end{pmatrix} \mu\text{T} \text{ and } \|\vec{B}_{Earth}\| = 48.8 \pm 9.3 \mu\text{T} \quad (23)$$

Even if the relative uncertainty on the calibration of the coils is small (less than 1%), the final error on the magnetic field measurement is rather large. This comes from the fact that in order to measure the small Earth field, we must apply a bias field that is much larger (of order of 2 mT on the z axis, i.e., 400 fold larger). As a result, a small error on the calibration of the coil field results in a large error on the Earth field measurement.

If we would like to reduce the uncertainty, two options can be considered:

- better calibration of the coils
- repeating this procedure with more values of the applied field



## 8. Noise analysis and system sensitivity calculation

The purpose of this part is to compare the noise contribution from the different subsystems of the KWANTEACH® Base setup.

### 8.1. Theoretical principles

#### 8.1.1. Laser noise

The laser intensity noise can be divided into two categories.

- Technical noise arises from any imperfection of the global laser system (noise of the pump source, mechanical vibrations, temperature variations, etc...)
- Quantum noise due to quantum the nature of the system, arising for instance from the corpuscular nature of light (shot noise).

#### 8.1.2. Optical Shot Noise

Photon shot noise generally represents the first fundamental limit one reaches in an experiment. It is therefore crucial to estimate its value to study the different limitations of a system. Photon shot noise is due to the corpuscular nature of light. The flow of photons emitted from the laser is irregular and follows Poisson statistics.



### 8.1.3. Photodetection noise

The sensitivity of a photodetector can be characterized by the Noise Equivalent Power (NEP) [18]. The NEP expresses the minimum detectable power by the photodetector per square root bandwidth. In other words, it is a measurement of the weakest optical signal that can be detected. Therefore, it is desirable to have a NEP as low as possible.

The NEP of a photodetector is obtained from its noise spectral density (NSD), divided by the gain of the photodetector, noted  $G$ . Note that the NEP, corresponds to the electronics shot noise associated with the photodetection dark current.

### 8.1.4. Noise analysis and sensitivity estimation

The purpose of this part is to compare the impact of the different noise sources in order to determine the limiting noise, and from that deduce the magnetic sensitivity of the system expressed in  $\text{T}/\sqrt{\text{Hz}}$ . As for the NEP of the photodetector, the magnetic sensitivity represents the smallest magnetic signal a magnetometer is able to measure in a 1 Hz bandwidth.



## 8.2. Experimental protocol

### 8.2.1. Estimation of the sensitivity

To obtain the best sensitivity, it is necessary to find an operating point where the fluorescence signal varies significantly with the magnetic field. Such an operating point can be found in the slope of a hyperfine level (see [Figure 54](#)). We define an operating point by the microwave excitation power and frequency, the external magnetic field and the laser power.



PARTIAL

### 8.2.2. Noise measurement

Estimating the magnetic sensitivity implies to acquire the system noise. In our system, the signal containing the measurement information is the NV centres photoluminescence.

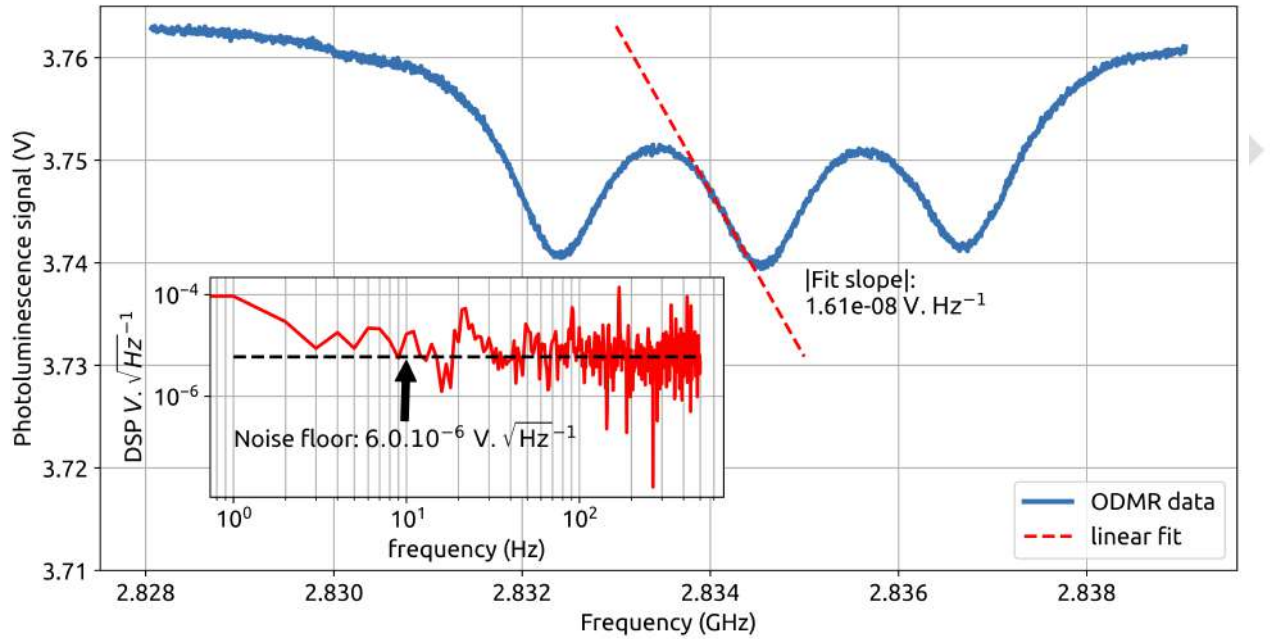


Figure 56. ODMR spectrum of a fine resonance including fitted resonance line slope. Insert: Noise acquisition of the NV photoluminescence KWANTEACH®.

### 8.3. Numerical applications

On one hand, the noise of the system can be estimated at  $6.0 \cdot 10^{-6} \text{ V}/\sqrt{\text{Hz}}$  plotted as a black horizontal dashed line in the insert of Figure 56. On the other hand, the steepest slope of the ODMR spectrum is (in absolute value)  $1.61 \cdot 10^{-8} \text{ V/Hz}$ . By multiplying by the gyromagnetic ratio of the NV centre of  $\gamma_{NV} \approx 28 \text{ GHz/T}$  we get  $1.61 \cdot 10^{-8} \times 28 \cdot 10^9 = 451 \text{ V/T}$ .

We can finally compute the magnetic sensitivity as the ratio of the previous two quantities, leading to:

$$\eta_B = \frac{6.0 \cdot 10^{-6}}{451} = 13 \text{ nT}/\sqrt{\text{Hz}} \quad (31)$$

It is also interesting to estimate the sensitivity one could reach if the system were only limited by the optical shot noise, the system noise limit is then given by Equation (26). In this case, we would have :



PARTIAL





## 9. Observation of strong-field level mixing

### 9.1. Theoretical principles

We here consider that a strong magnetic field  $B_{\perp}$ , perpendicular to the NV axis, is applied to the NV centre. For such a field, the nature of the levels is modified, thus influencing the different level couplings and facilitating population transfers between certain levels, as explained in [Introduction](#).

### 9.2. Experimental protocol

PARTIAL



PARTIAL





⑫ Pulsed photodetector

PARTIAL



PARTIAL



PARTIAL



PARTIAL



## 11. Saturation of NV centers

### 11.1. Theoretical principles

As mentioned previously, the fluorescence from the NV centres subjected to the strongest laser intensity is detected at the output of the monomode fibre. However, because it can be considered as a two energy levels system, the NV centre fluorescence emission does not increase infinitely but reach a maximum called saturation power. This phenomenon is directly linked to the radiative lifetime of the excited levels as well as to the absorption cross section of the NV centres.

### 11.2. Experimental protocol

The saturation curve of the NV centres can be obtained by plotting the fluorescence light power (red) versus that of the excitation beam (green). We measure the level of red photoluminescence via the photodetector, whose *Voltage* to *Optical Power* conversion is known. To perform the measurement, we need the widest possible laser power range.



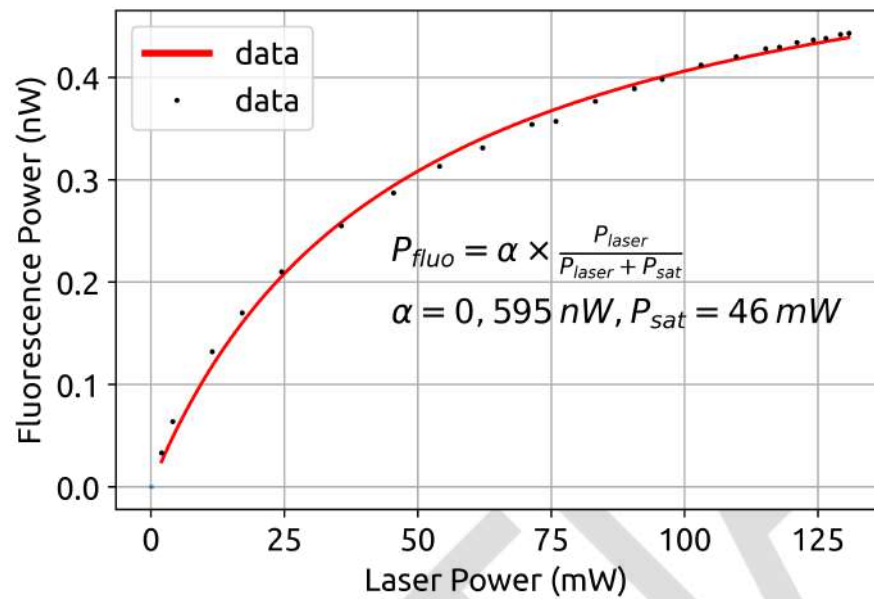


Figure 66. Saturation curve of NV centres obtained with the KWANTEACH® pulsed module.

The saturation power  $P_{sat}$  allows us to characterize the pumping efficiency of our setup and is also linked to the electron spin resonance contrast. For further information, one can read in details [22].



## 12. Polarisation and relaxation time $T_1$ of the NV centre

### 12.1. Theoretical principles

#### 12.1.1. Energy levels and explanation of the principle of polarisation

The NV<sup>-</sup> centre has a global electronic spin  $S = 1$ , associated with two unpaired electrons. The fundamental and excited levels are thus electron spin triplets, characterized by the quantum number  $m_s$  which can take the values  $-1, 0, 1$  depending on the projection of the spin on the quantization axis. Due to the symmetry of the NV centre, the natural quantization axis is the NV axis. The degeneracy between the states  $|m_s = \pm 1\rangle$  and  $|m_s = 0\rangle$  is partially lifted by the spin-spin interaction. The states  $|m_s = \pm 1\rangle$  and  $|m_s = 0\rangle$  are thus separated by frequencies of  $D_{\text{ground}} = 2.87$  GHz in the ground state and  $D_{\text{excited}} = 1.42$  GHz in the excited state.



### 12.1.2. Principle of a measurement sequence

The first step for measuring  $T_1$  is to prepare the NV in an out of equilibrium state, such as  $|m_s = 0\rangle$ . Optical pumping via an incident laser on the diamond drives the population in the state  $|m_s = 0\rangle$  after a certain number of cycles, as explained previously. Once prepared in this state, the laser beam is switched off to allow a return to thermodynamic equilibrium and a Boltzmann distribution. It is possible to observe optically and directly this relaxation of the "bright" state  $|m_s = 0\rangle$ , towards a distribution with the "dark" states  $|m_s = \pm 1\rangle$ . The measurement of  $T_1$  is performed by repeating a polarization-measurement sequence.



## 12.2. Experimental protocol

In this section, we present the measurement of the longitudinal spin relaxation time  $T_1$  with the KWANTEACH® setup.

### 12.2.1. Duration of the laser pulse

PARTIAL



### 12.2.2. Laser intensity and polarization time



### 12.2.3. Influence of the extinction time

## 12.2.4. Integration parameters

The time resolved acquisition of the NV spin state is obtained by varying the dark time in the sequence described in [Figure 68](#). The spin-state readout is performed by averaging the signal at the beginning of the pulsed, and normalizing it by the signal at the end of the pulse, where the NV is re-polarized in the  $|m_s = 0\rangle$  state. In this section, we explain how to set the position and duration of the different integration regions, at the beginning and at the end of the pulse.

### 12.2.4.1. Integration Offset

The *Integration Offset Beginning* parameter corresponds to the time interval between the start of the pulse and the beginning of the first integration zone. Similarly, the *Integration Offset End* parameter corresponds to the time interval between the end of the second integration zone and the end of the pulse.



#### Integration time

Finally, the *Integration* parameter, expressed in % or seconds, defines the duration of the integration zones. This integration time is expressed in percentage relative to the total duration of the laser pulse. The choice of its value is a compromise between the contrast of the  $T_1$  curve and the noise on the measurement. A correct value to obtain high contrast with not too much noise, meaning a good SNR, would be about 10%.

#### 12.2.5. $T_1$ measurement

We have now seen the impact of all the sequencer parameters, and found the optimal values for our bulk diamond sample. We can proceed to a measurement, for example with the following sequence parameters:



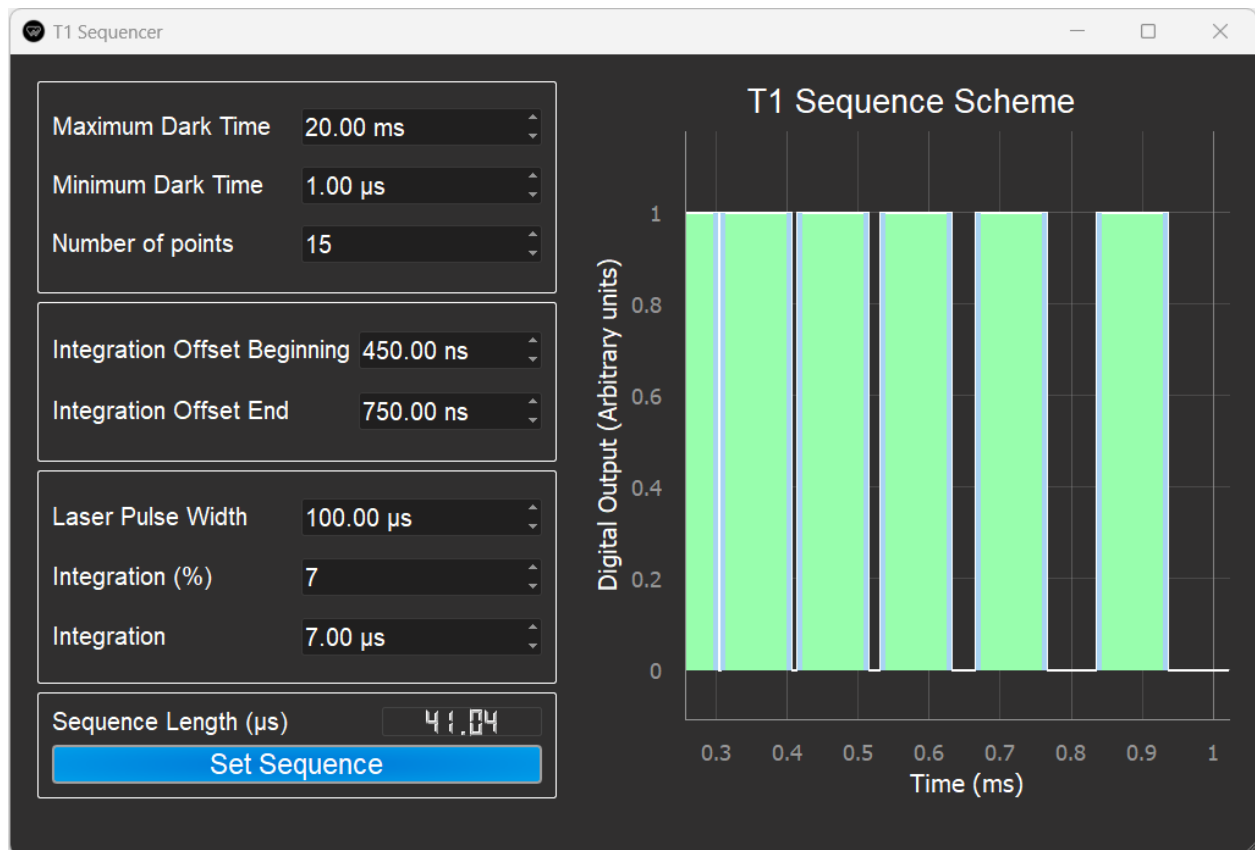


Figure 73.  $T_1$  sequencer with optimal params for the given bulk, volume-doped diamond. On the right, the end of the sequence, with the laser pulse in green and their associated integration areas in grey.

If the setup is correctly aligned, and the signal on the photodetector of the KWANTEACH® Pulsed is sufficiently high, one shall obtain a curve such as the following Figure 74.

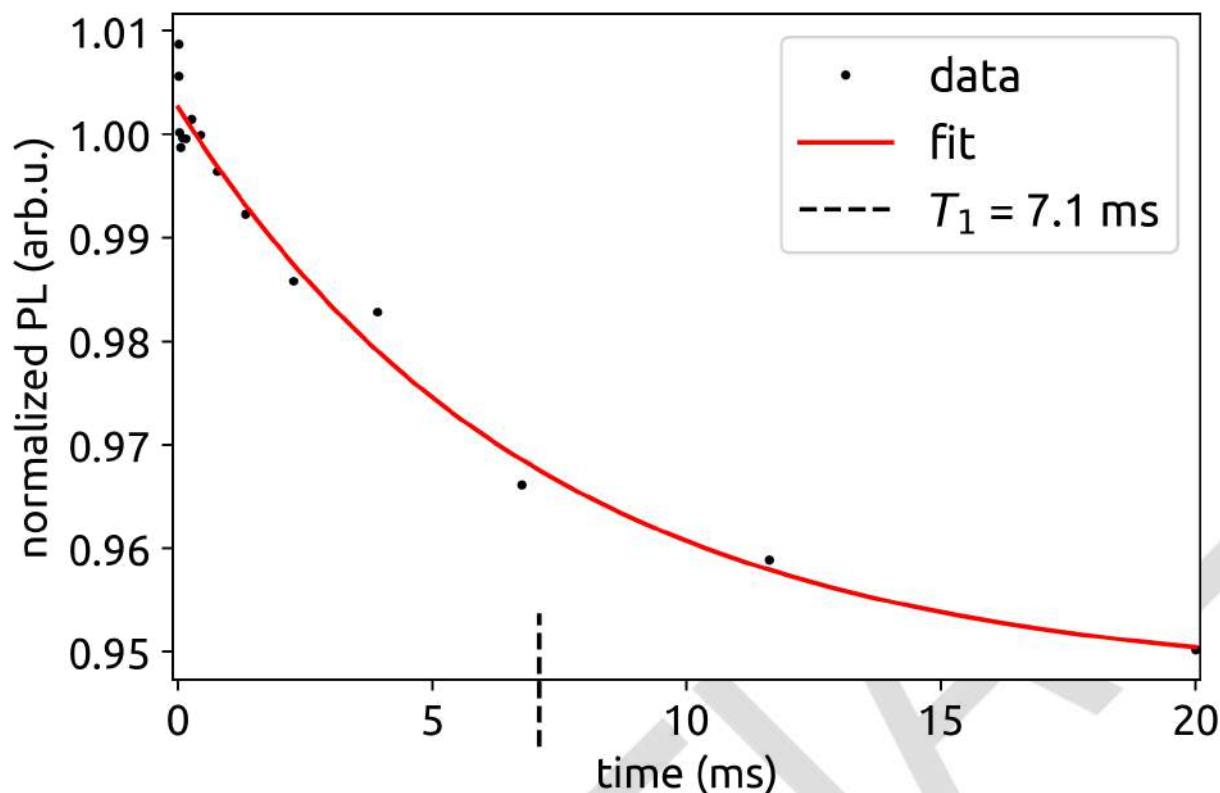


Figure 74. Resulting  $T_1$  curve, with an exponential fit over the raw data. The obtained  $T_1$  value is 7.1 ms.

This curve describes as expected the exponential decay from the  $|m_s = 0\rangle$  state to the equilibrium. For the given samples, the time constant  $T_1$  is expected to be of a few milliseconds. The fit is performed using a decaying exponential function, with a characteristic time of  $T_1$ , whose expression is similar to:  $A(1 - Ce^{-\frac{t}{T_1}})$ , with  $A$  being the amplitude of the signal (normally close to 1),  $C$  a contrast parameter, and  $\tau$  the dark time.

To go further with this experiment, the influence of different physical parameters on  $T_1$  could be studied, and notably by creating a magnetic noise close to the NV transition, like described in reference [26].



PARTIAL



## 13. Microwave Pulse Delay Calibration

### 13.1. Context

The following part will deal the calibration of your modulation system, a required step for this kind of setup. The KWANTEACH® include two of them:

- ① The Acousto-Optic Modulator (AOM), to perform laser pulses;
- ② The Microwave (MW) chain, to perform the microwave pulses.

For the following experiment, time gap between those two-pulse emitter must be known precisely and controlled. Indeed, an unwanted overlap or an imprecision on the pulse's duration would induce unwanted spin modification and degrade the measurement. Those troubles could occur because of a different propagation time in the two modulation systems.



PARTIAL



## 14. Rabi Oscillations

### 14.1. Theoretical principles

In the case of a system with two energy levels, the application of a magnetic field to the resonant frequency of the transition causes a coupling with the eigenstates of the system: the two initial eigenstates are then no longer stationary solutions of the Hamiltonian. A NV centre initially in  $|m_s = +1\rangle$  or  $|m_s = 0\rangle$  therefore oscillates between the two levels, as described in [Figure 76](#).

### 14.2. Rabi oscillations with NV centres ensemble

#### 14.2.1. Acquisition of Rabi oscillations

For the NV centre, it is necessary to apply a field to lift the degeneracy of the  $|m_s = \pm 1\rangle$  levels, and then to acquire a magnetic resonance spectrum to find the frequency of the transition chosen to obtain Rabi oscillations in a two-level system. The sequence is described in the [Figure 77](#) below.

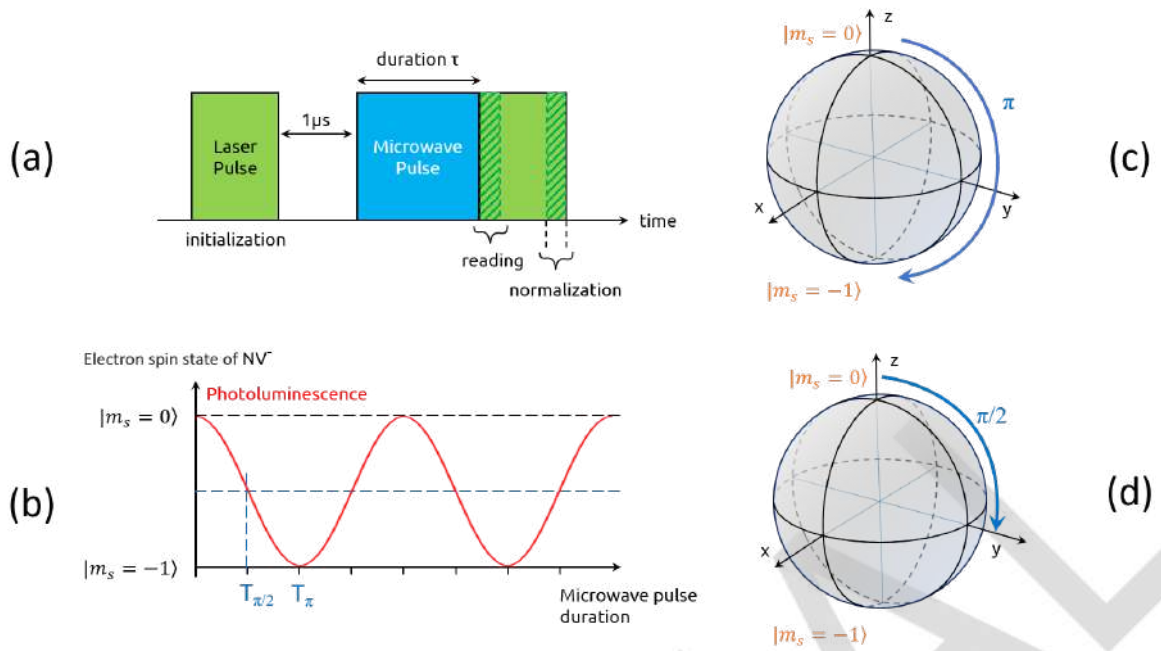


Figure 77. (a) Rabi sequence with the laser pulses and the ramping microwave pulse duration in between. (b) Rabi oscillations figures, with  $\pi$  and  $\frac{\pi}{2}$  microwave pulse duration, not taking into account decoherence. (c) and (d) Respectively  $\pi$  and  $\frac{\pi}{2}$  microwave pulses in the Bloch sphere. The first one transfer the whole population from state  $|m_s = 0\rangle$  to  $|m_s = -1\rangle$ , while the second creates a linear combination of the two states.

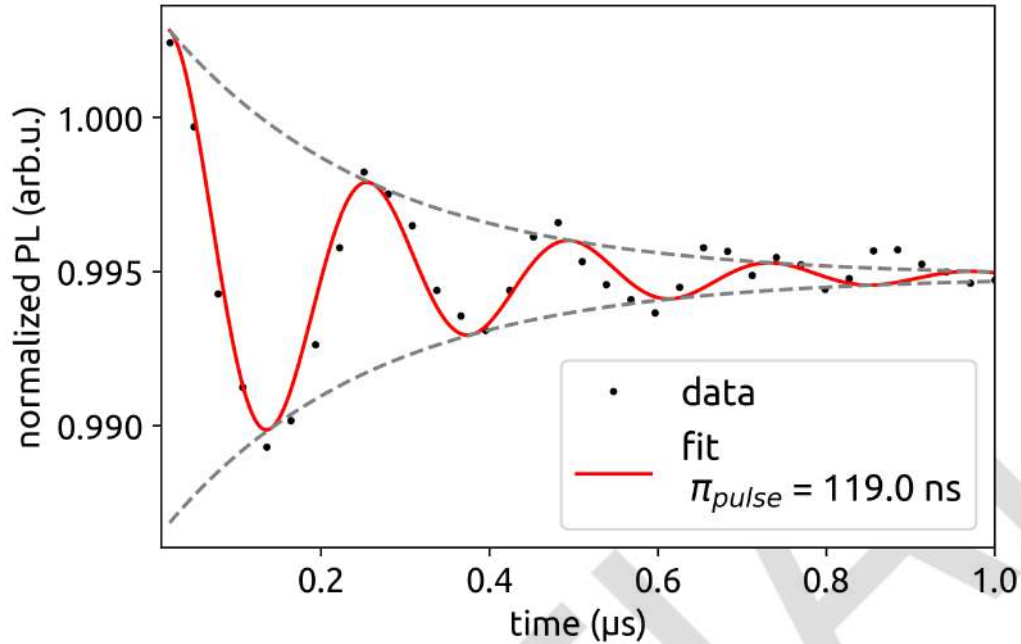


Figure 78. Rabi oscillations measured on the setup. The  $\pi$  pulse duration is approximately 119 ns.

Typical parameters to be chosen to obtain such a result would be those shown in Figure 79.

Note that the *Laser Pulse Width* and its associated *Integration Length* must be adjusted to best fit the polarisation of the NV centres on your setup. The  $\frac{\lambda}{2}$  can be rotated to adjust the laser and thus, the *Laser Pulse Width*. You should not go for too short pulses to avoid heating effect in the AOM module which would degrade the quality of your rising/falling pulse edges and therefore of your measurement.

MW Frequency	2.89166 GHz
MW Power	27.5 dBm
Maximum MW pulse	1.00 μs
Minimum MW pulse	20.00 ns
Number of points	35
Integration Offset Beginning	450.00 ns
Integration Offset End	750.00 ns
Laser Pulse Width	100.0 μs
Integration (%)	7
Integration	7.00 μs

Figure 79. Rabi Sequencer window, with typical parameters to obtain a curve as the previous figure.





### 14.2.2. Microwave power influence on Rabi oscillations

Considering the expression of the Rabi pulsation  $\Omega_R = \frac{1}{\sqrt{2}}\gamma_e B_{\text{pulse}}$ , we can expect an increase of the oscillation's frequency with the microwave field amplitude. To observe this behaviour, we can acquire Rabi oscillations for various microwave setpoint and measure its associated period. In our system, the microwave is set as a power, thus one should plot the square of the period as a function of this microwave power.

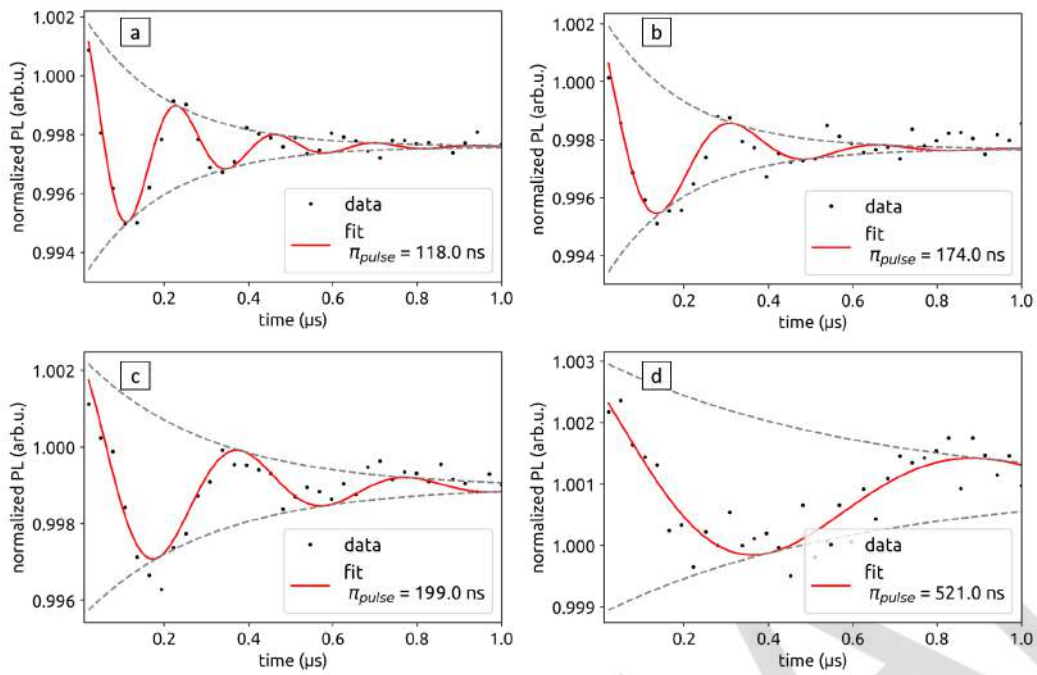


Figure 81. Rabi oscillations at four different RF power levels, showing the influence of this parameter on the  $\pi$  pulse duration. (a): 22 dBm, (b): 18.5 dBm, (c): 15.5 dBm, (d): 9 dBm.

Figure 81 shows the Rabi oscillations for different values of the microwave pulse power for a chosen microwave frequency. As long as the microwave frequency is tuned to a hyperfine transition the oscillations period is only driven by the microwave field amplitude. In the following section we will see that the frequency detuning has an influence on the oscillations period.

### 14.2.3. Microwave detuning influence on Rabi oscillations



PARTIAL



## 15. Ramsey fringes

### 15.1. Theoretical principles

Decoherence is the loss of information in a system initially placed in a state of quantum superposition, in our case  $|\psi\rangle = \frac{1}{\sqrt{2}}|m_s = 0\rangle + \frac{1}{\sqrt{2}}|m_s = \pm 1\rangle$ .

The Ramsey fringes method allows us to probe the transverse coherence time  $T_2^*$  of the system under the influence of its environment [32], during its free precession.

PARTIAL



PARTIAL



PARTIAL



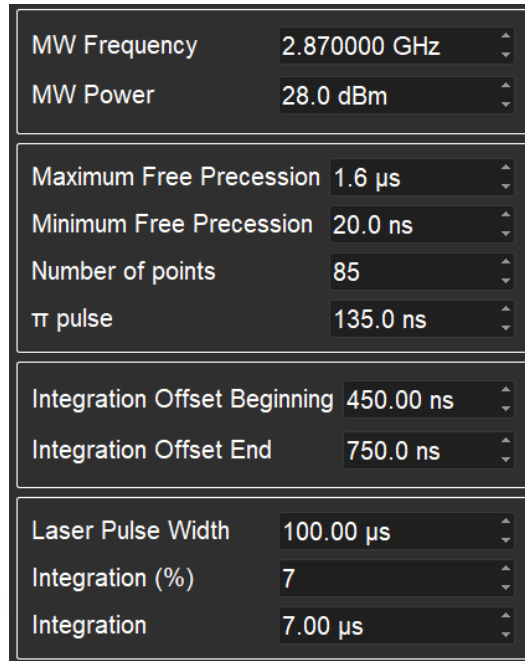
PARTIAL

## 15.2. Experimental protocol

### 15.2.1. Acquisition of Ramsey fringes

#### 15.2.1.1. Parameters of the experiment

Typical parameters to be chosen to obtain Ramsey fringes would be those shown in [Figure 88](#). All remarks made previously on the *Rabi Pulsed Experiment* chapter concerning the laser pulse are still valid.

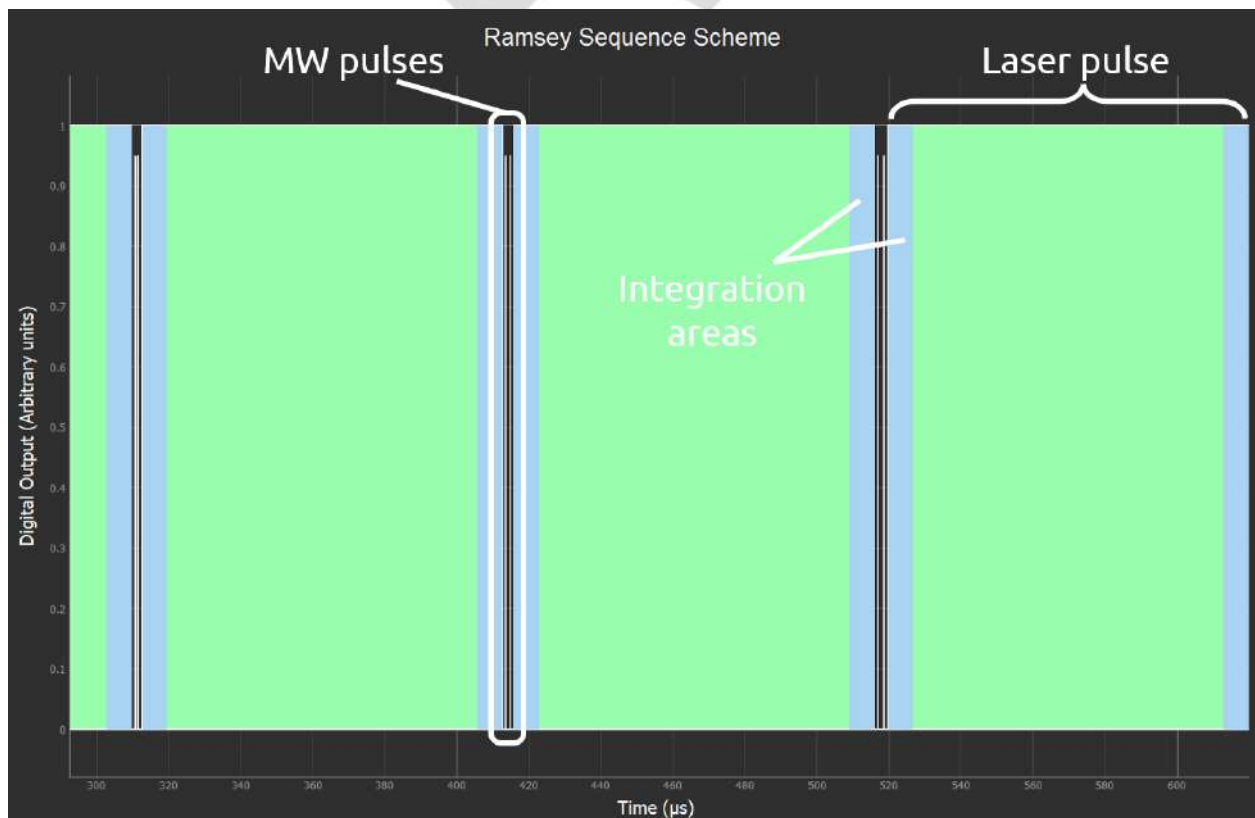


MW Frequency	2.870000 GHz
MW Power	28.0 dBm
Maximum Free Precession	1.6 $\mu$ s
Minimum Free Precession	20.0 ns
Number of points	85
$\pi$ pulse	135.0 ns
Integration Offset Beginning	450.00 ns
Integration Offset End	750.0 ns
Laser Pulse Width	100.00 $\mu$ s
Integration (%)	7
Integration	7.00 $\mu$ s

*Figure 88. Ramsey Sequencer window, with typical parameters to obtain a curve as the previous [Figure 86 \(b\)](#).*



Once you have chosen all the parameters, click on *Set Sequence* button. You can look in detail at your sequence in the graph, as in [Figure 90](#). The laser pulses are shown in green, with their areas of integration. The MW pulses are plotted in red.



### 15.2.1.2. Measurement of Ramsey fringes

Depending on the MW frequency, with respect to the position of hyperfine levels, we can obtain a resulting signal of two or three beating transitions.

A good result would be the [Figure 91](#) below, obtained with similar parameters as in [Figure 88](#) for the central hyperfine. The fit is obtained with the product of a decaying exponential  $\exp^{-\frac{t}{T_2^*}}$  and the sum of three (or two) cosines  $B \cos(2\pi f_n t + \phi_n)$ , each with its frequency  $f_n$  and phase  $\phi_n$ . This last one is let as a parameter because we do not expect our MW  $\pi$  pulse to be perfectly phased with the hyperfine transitions, meaning it will not be in the equatorial plane of the Bloch sphere. The results are shown in red for the fit, and dashed grey for the envelop on [Figure 91](#) and [Figure 93](#).

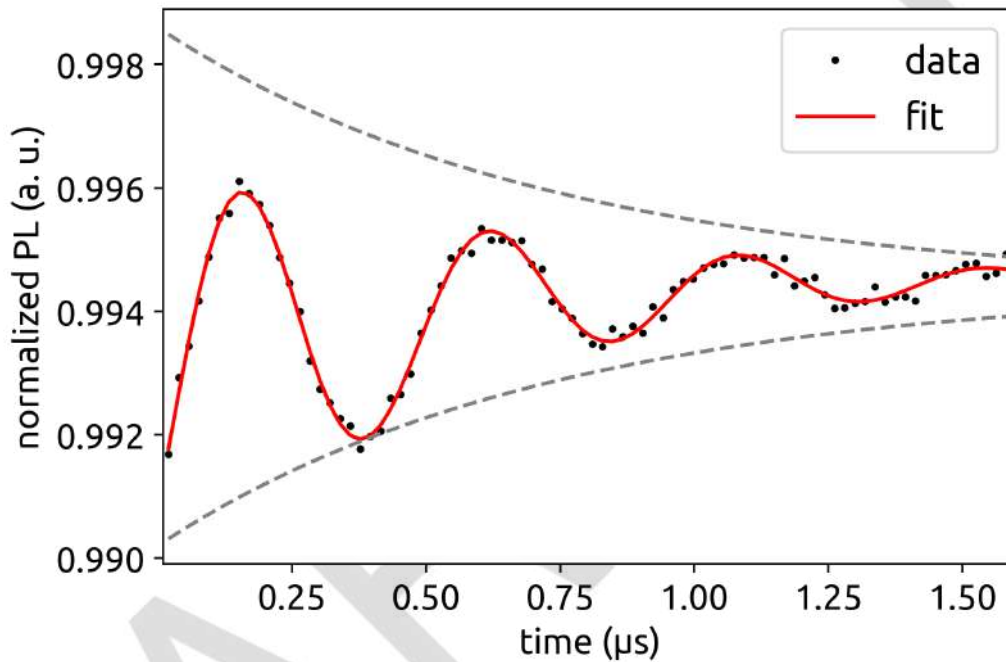


*Figure 91. Ramsey fringes when the MW frequency address the central hyperfine transition, showing a result of the beating of two sinus. The decaying envelop is seen in dashed grey, with a  $T_2^*$  of  $\sim 600$  ns.*

For the first measurement shown on [Figure 91](#), we have pointed the central hyperfine transition. The Power Spectral Density (PSD) of the Ramsey Signal shows us the contribution of each transition in the hyperfine structure. We get here only two contributions: those of the lateral and the central lines, as shown on [Figure 92](#). The position of the main peak in the PSD is like expected around 2.1 MHz. The smaller peak corresponds to the contribution of the central hyperfine, and it is not well resolved because of its low frequency. Furthermore, the Full Width at Half Maximum (FWHM) indicate an order of magnitude of the  $T_2^*$ , with  $\text{FWHM} \propto \frac{1}{\pi T_2^*}$ . The expected values for the given sample is of a few hundreds of nanoseconds, and close to what the fit gave us on the previous [Figure 91](#).

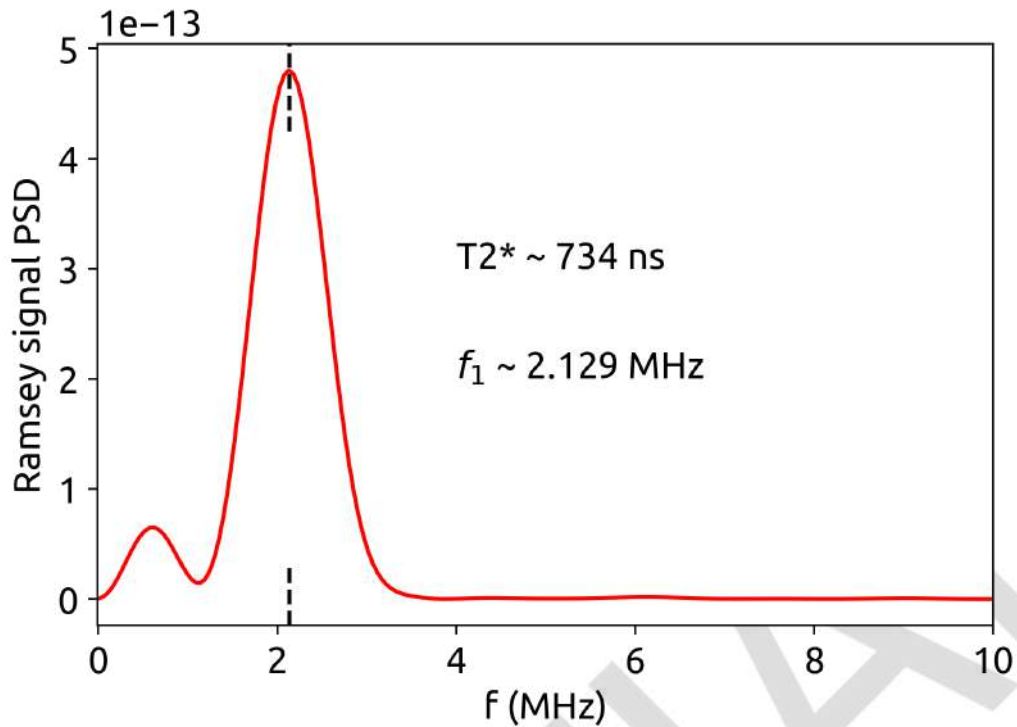


Figure 92. PSD of the above curve Figure 91. We see the two-frequency contribution that result in a beating. The FWHM indicate an order of magnitude of the  $T_2^*$ . The frequency difference between the two peaks is close to the hyperfine oscillation frequency.

On the second example, the contribution of the three transitions is seen on Figure 94 as we have pointed out the lateral line for this measurement. The parameters are the same, to the exception of the MW frequency.

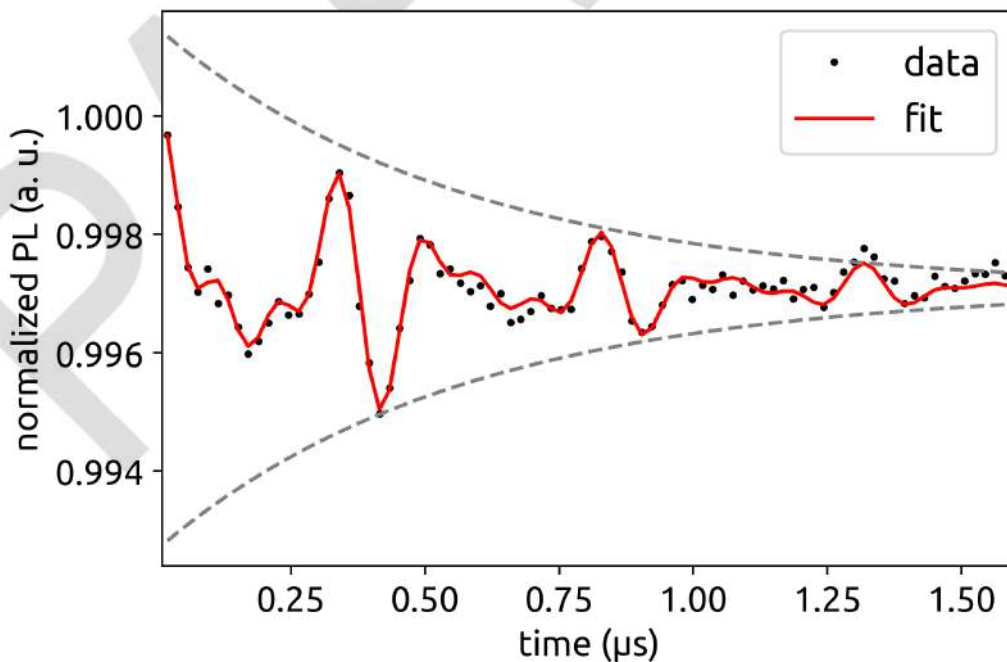
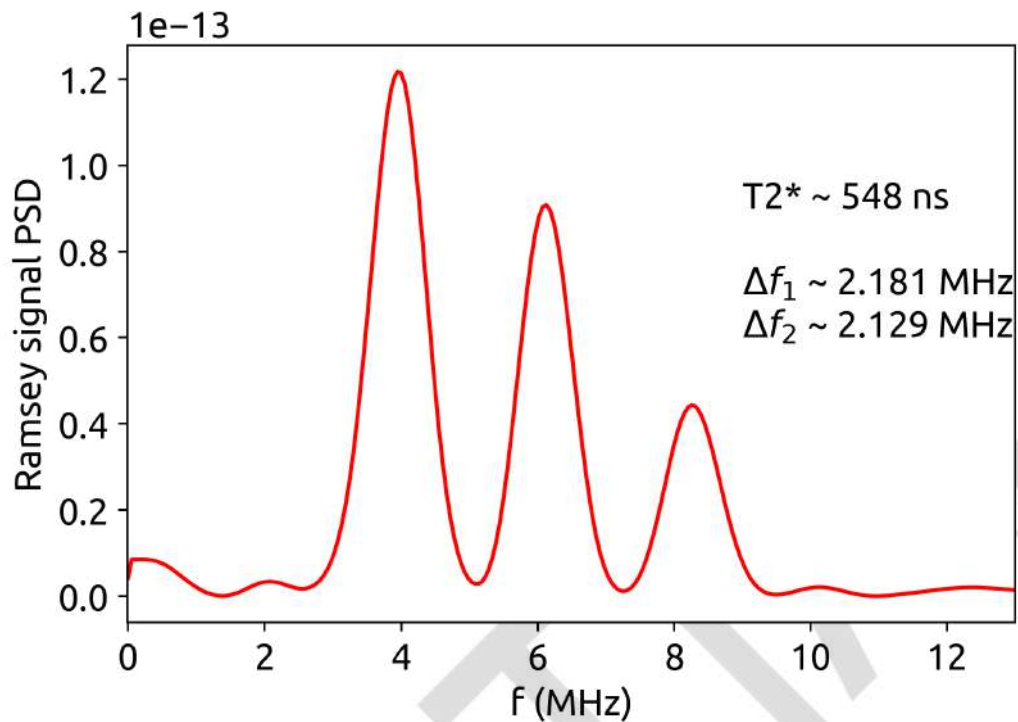


Figure 93. Ramsey fringes when the MW frequency address one lateral hyperfine transition, showing a result of the beating of three sinus.

We look again at the PSD of the signal in [Figure 94](#). The result is a three-peak distribution, each one separated by  $\sim 2.15\text{MHz}$ , the hyperfine frequency. The first peak at  $f_1 \approx 4\text{MHz}$ , reveals the detuning of our MW with respect to the lateral hyperfine.



*Figure 94. PSD of the above curve [Figure 93](#). We see here the three contribution of the hyperfine levels that results in a complex beating. The frequency difference between the central and the lateral peaks is  $\sim 2.15\text{MHz}$ .*

For further reading and more complex experiments, one can look at [\[32\]](#) thesis.

As explained before, the limitation of the  $T_2^*$  has two origins, the homogeneous and the inhomogeneous contributions. This homogeneous dephasing can be suppressed with dynamic decoupling sequence, one of the simplest being the Hahn Echo experiment described in the next chapter.



## 16. Spin Echo

to be released...

PARTIAL

## 17. Contact information

**Company name:** Kwan-Tek

**Company address:**

1 rue Galilée, Batiment Innova

Parc technologique de Soye

56270 Ploemeur

FRANCE

**Technical support:** [kwanteach.support@kwan-tek.com](mailto:kwanteach.support@kwan-tek.com)

**Sales department:** [sales@kwan-tek.com](mailto:sales@kwan-tek.com)

**Website:** <https://www.kwan-tek.com>

